

# The dynamical phase transitions of stellar systems and the corresponding kinematics

Xufen Wu<sup>1</sup>, Pavel Kroupa<sup>1,2</sup>

<sup>1</sup> *Argelander-Institut fuer Astronomie der Universität Bonn, Auf dem Hügel 71, D-53121 Bonn, Germany*

<sup>2</sup> *Helmholtz-Institut für Strahlen-und Kernphysik, Universität Bonn, Nussallee 14-16, D-53115 Bonn*

13 October 2021

## ABSTRACT

External fields in Milgromian dynamics (MD or MOND, Milgrom 1983) break the Strong Equivalence Principle (SEP) and change the dynamics of self-bound stellar systems moving in space-varying background gravitational fields. We study two kinds of re-virialisation of the stellar systems: the violent phase transition and the adiabatic phase transition for systems moving on radial orbits, where the external field evolves from strong to weak and whose corresponding dynamics changes from Newtonian to Milgromian. We find that the time scale for the phase transformation from Newtonian to Milgromian gravity lies only within one to a few crossing times for low density globular clusters with masses ranging from  $10^4 M_\odot$  to  $10^6 M_\odot$ . Thus a globular cluster can appear frozen in the Newtonian regime despite being in the Milgromian regime for not longer than a few crossing times. We also study the kinematics and anisotropy profiles of the systems. The velocity dispersions of the systems are larger after the phase transitions, especially for the outer regions of the stellar systems. Moreover, the isotropic systems become radially anisotropic, especially for the outer parts, after the process caused by the dynamical phase transition. Deeper Milgromian systems have more radially anisotropic velocity dispersion functions. We also find that the final profiles of density, velocity dispersion and anisotropy do not depend on the details of the phase transition. I.e., the mass distribution and kinematics of the end-states of the globular clusters do not depend on the rapidity of the transition from Newtonian to Milgromian gravity. Thus, the transition from the Newtonian to the Milgromian regime naturally induces a significant radially anisotropic velocity distribution in a globular cluster.

**Key words:** galaxies: kinematics and dynamics - methods:  $N$ -body simulations - (Galaxy:) globular clusters: general

## 1 INTRODUCTION

Milgrom’s dynamics (hereafter MD, Milgrom 1983) links the gravity in galaxies with the baryonic distribution, without Cold or Warm Dark Matter. The original Bekenstein-Milgrom’s equation (Bekenstein & Milgrom 1984) is fully predictive on galactic scales: the baryonic Tully-Fisher relation (Tully & Fisher 1977), the shapes of rotation curves of low and high surface brightness galaxies (Milgrom & Sanders 2003; Sanders & Noordermeer 2007), the dark matter effect in tidal dwarf galaxies (Gentile et al. 2007), a universal scale of baryons and dark matter at the core radius of effective dark matter (Gentile et al. 2009), the faster rotation speeds in polar rings (Lüghausen et al. 2013). Besides the success on the galactic scale, a cosmological model based on MD with massive sterile neutrino was proposed recently (Angus 2009; Angus & Diaferio 2011), which

matches the matter power spectrum, forms the right order of magnitude number of X-ray clusters and forms the high relative speeds of pairs of halos like the Bullet Cluster. It is important to keep MD as a realistic option for small scale gravitational astrophysics because the Newtonian approach is problematic (Kroupa et al. 2010; Kroupa 2012; Kroupa et al. 2012). MD is essentially a dark matter theory with 100% conspiracy of phantom dark matter with baryons: the baryons dictate via the field equation how much phantom dark matter should be in a stellar system (Bekenstein & Milgrom 1984; Famaey et al. 2007; Wu et al. 2007),

$$-\nabla \cdot [\mu(X)(\mathbf{g}_{\text{ext}} - \nabla\Phi_{\text{int}})] = 4\pi G\rho, \quad (1)$$

$$X = \frac{|\mathbf{g}_{\text{ext}} - \nabla\Phi_{\text{int}}|}{a_0}.$$

Here  $a_0$  is Milgrom’s (1983) acceleration constant and we use  $a_0 = 3.7 \text{ pc Myr}^{-2}$ . The above equation shows that the internal dynamical potential  $\Phi_{\text{int}}$  of a gravitating system in MD depends on the baryon density  $\rho$  and its acceleration  $\mathbf{g}_{\text{ext}}$  in the external background field, even if the latter is constant and uniform. The interpolating function  $\mu$  satisfies

$$\begin{aligned} \mu &\rightarrow X \quad (X \ll 1), \\ \mu &\rightarrow 1 \quad (X \gg 1). \end{aligned} \quad (2)$$

This ensures that the internal gravity acceleration  $\mathbf{g}_{\text{int}}$  is Newtonian when  $X \gg 1$  and is in the deep MD regime when  $X \ll 1$ . The external field  $\mathbf{g}_{\text{ext}}$  truncates the logarithmic potential of an isolated Milgromian system and enables stars to escape. In contrast to the Newtonian case, because the dynamics of a system depends on both internal and external fields, the Strong Equivalence Principle (SEP) is violated in MD. The function  $\mu$  can be derived from quantum mechanical process in space time (Milgrom 1999; Kroupa et al. 2010, Appendix A). Milgrom’s dynamics is thoroughly reviewed by Famaey & McGaugh (2011).

The external field effect (EFE) has been studied for a variety of situations: the absence of dark matter in star clusters in the inner Milky Way disc (Milgrom 1983), the motion of probes in the inner solar system (Milgrom 2009; Iorio 2010), the Roche lobes of binary systems (Zhao & Tian 2006), the escape speeds and truncations of galactic rotation curves (Wu et al. 2007), the distant star clusters of the Milky Way (Haghi et al. 2011) and line-of-sight velocity dispersion of satellites surrounding a host galaxy (Angus et al. 2008).

MD predicts that a self-bound gravitational system moving in a space-varying field should have varying internal dynamics, especially for diffuse systems. Stellar systems like low-central-density globular clusters and ultra-faint dwarf satellite galaxies are the best candidates to test gravitational dynamics. Those systems moving from the galactic centre to the outer parts should change their internal gravity from Newtonian to Milgromian. Therefore such systems are not in equilibrium when moving on such orbits, and there is an additional evolution of such systems. In this paper we are interested on the time scale the systems re-virialise, and their morphology and internal kinematics when the background field changes.

We construct models for low-central-density stellar systems with different parameters that are allowed by observations, and study their evolution during the violation of the SEP via: (1) violent process of the SEP violation by shifting the gravity suddenly from Newtonian to deep MD in §3; (2) moving the systems on realistic radial orbits in the Milky Way Besonçon Milgromian potential (Wu et al. 2008) in §4 and §4.4. We conclude our results in §5.

## 2 EXTENDED GLOBULAR CLUSTERS

Globular clusters (GCs) are typically compact objects with half-light radii of a few pc and with masses in the range  $10^4 - 10^6 M_\odot$ . The internal gravitational fields in the compact centres of normal GCs are usually much larger than Milgrom’s acceleration constant  $a_0$ , hence the normal GCs are dominated by Newtonian gravity, and they are not good candidates to test the dynamics of alternative gravities. However

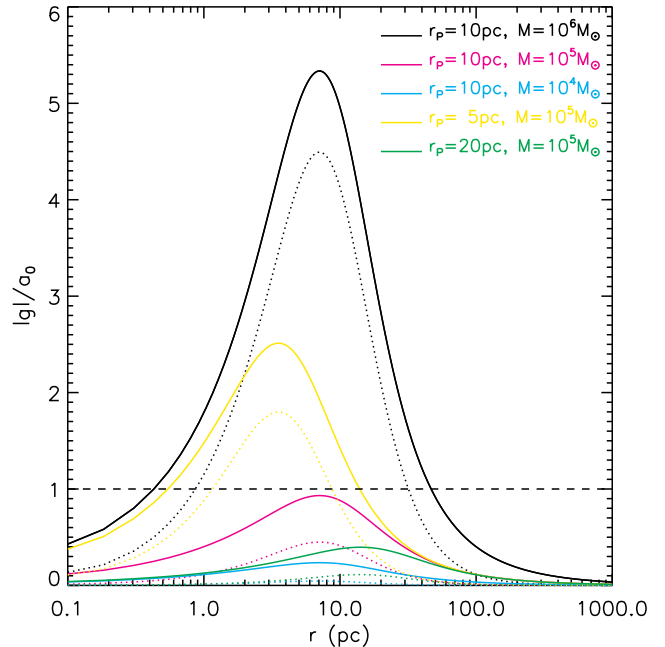


**Figure 1.** The gravitational acceleration for the models in Table 1. The solid and dotted lines are acceleration from the Milgromian and Newtonian Poisson equations, respectively. The dashed line is  $a_0 = 3.7 \text{ pc Myr}^{-2}$ .

there is a certain fraction of GCs ( $\approx 9\%$  for the Galactic GCs in Harris 1996) that have extended half-light radii of more than 10 pc. The extended GCs are found widely existing around extragalactic systems and their half-light radii can reach up to 30 pc (Larsen & Brodie 2000; Harris et al. 2002; Chandar et al. 2004; Lee et al. 2005; Peng et al. 2006; Chies-Santos et al. 2007; Georgiev et al. 2009; Huxor et al. 2011; Brüns & Kroupa 2011; Bruens & Kroupa 2012, in preparation). In contrast to normal GCs, the extended GCs have low density centres, where the acceleration in the central regions can be below  $a_0$ . Therefore it is very important to test the dynamics of the extended GCs in different gravities. A test of the outer Galactic clusters is suggested by Baumgardt et al. (2005), with the assumption that the velocity dispersion profiles in the clusters are isotropic.

We use Plummer’s density profile (Plummer 1911; Binney & Tremaine 2008) to model the extended GCs,

$$\rho(r) = \frac{3M}{4\pi r_P^3} \left(1 + \frac{r^2}{r_P^2}\right)^{-5/2}, \quad (3)$$

where  $r_P$  is the scale radius and has a relation with half mass radius  $r_h \simeq 1.3 r_P$ ,  $M$  is the total mass. We use the method of Gerhard (1991) to construct isotropic N-body Initial Conditions (ICs) in Newtonian gravity for the violent re-virialisation simulations. We summarise the parameters of the mass models in Table 1, and the parameter  $N$  in Table 1 is the number of N-body particles. The accelerations of the analytical mass models (not from the N-body particles) obtained from the Milgromian (Eq. 1) and Newtonian Poisson equations are shown in Fig. 1. We find that the mass models 2, 3 and 5 are in the deep MD regime while model 1

**Table 1.** Parameters of isolated mass models for extended globular clusters. The columns from left to right provide the following information of the models: models' ID (1<sup>st</sup> column), total mass (2<sup>nd</sup> column), Plummer radius  $r_P$  (3<sup>rd</sup> column), number of particles in the simulations (4<sup>th</sup> column), crossing time of models in Newtonian gravity (5<sup>th</sup> column) and in Milgromian gravity (6<sup>th</sup> column), a characteristic time scale for the Milgromian Plummer model  $r_P(GMa_0)^{-1/4}$  (7<sup>th</sup> column), the stability parameter  $\xi$  of the models after re-virialised (8<sup>th</sup> column) and the corresponding colours used in Fig. 1 (9<sup>th</sup> column).

Models ID	$M(M_\odot)$	$r_P$ (pc)	N	$T_{\text{cross}}^{\text{Newt}}$ (Myr)	$T_{\text{cross}}^{\text{MD}}$ (Myr)	$r_P(GMa_0)^{-1/4}$ (Myr)	$\xi$	Colour
1	$10^6$	10	100000	3.53	2.73	0.89	1.11	Black
2	$10^5$	10	100000	11.69	5.70	1.58	1.65	Magenta
3	$10^4$	10	25000	36.58	10.42	2.81	2.26	Cyan
4	$10^5$	5	100000	4.07	2.72	0.79	1.25	Yellow
5	$10^5$	20	100000	32.53	11.70	3.16	2.37	Green

is mostly ( $r < 5r_P$ ) in the Newtonian regime, and model 4 is dominated by mild-Milgromian gravity.

### 3 VIOLENT PHASE TRANSITION

The most direct way to study the phase transition in different gravities is virialising the Newtonian equilibrium models with the Milgromian Poisson equation (Eq. 1). A GC which is shot from the galactic centre to the outer regime, if the Galactic orbital time is much shorter than the re-virialisation time scale, experiences such a violent dynamical phase transition.

#### 3.1 Numerical setup

The interpolating function  $\mu(X)$  has several popular forms giving the same asymptotic behavior in Eq. 2. We shall apply the ‘simple’- $\mu$  function in the following of this paper (Famaey & Binney 2005; Sanders & Noordermeer 2007; Wu et al. 2007),

$$\mu(X) = X/(1 + X). \quad (4)$$

In order to solve the non-linear Poisson equation (Eq. 1), we use the particle-mesh N-body code NMODY (Londrillo & Nipoti 2009). NMODY is developed for isolated Milgromian gravity systems and has been well tested (Nipoti et al. 2007, 2008, 2011). It solves Newtonian potentials by the spherical harmonic expansion to the differential Poisson equation and then iterates into the Milgromian potential. For the simulations in this section, we choose a grid-resolution of  $n_r \times n_\theta \times n_\phi = 256 \times 32 \times 64$ , where  $n_r$ ,  $n_\theta$ ,  $n_\phi$  are the number of grid cells in radial, polar and azimuthal dimensions, respectively. The radial grids are defined as  $r_i = r_s \times \tan [(i + 0.5)0.5\pi/(n_r + 1)]$  with  $r_s = 20$  pc and  $i = 0, 1, 2, \dots, n_r$ , and the angular grids are equally segmented. NMODY uses the leap-frog scheme to integrate the motions of the particles. The time steps are globally defined as  $\mathbf{dt} = \frac{0.1}{\sqrt{\max |\nabla \cdot \mathbf{g}_{\text{int}}|}}$ , meaning that there are around 10 time steps on an orbital loop for the particles in the densest regime. Therefore the time steps are small enough to avoid the artificial run-aways of the particles in the central regime.

In order to choose the correct time scale for our simulations, we define the crossing time of the models in this paper as  $T_{\text{cross}} = r_{90}/v_{\text{circ},r_{90}}$ , where  $r_{90}$  is the radius enclosing 90% of the total mass of a model, and  $v_{\text{circ},r_{90}}$  is

the corresponding circular velocity. In Newtonian dynamics,  $v_{\text{circ},r_{90}}^{\text{Newt}} \equiv \sqrt{GM_{90}/r_{90}}$ , where  $M_{90}$  is 90% of the total mass, while  $v_{\text{circ},r_{90}}^{\text{MD}} \equiv (GM_{90}a_0)^{1/4}$  in Milgromian dynamics. The crossing time is the time scale within which the majority of a system virialises. The values of  $T_{\text{cross}}^{\text{Newt}}$  (i.e., crossing times of the Newtonian models) are listed in Table 1. The crossing times of the models range from 3.5 to 36.7 Myr. The corresponding two-body relaxation times are  $t_{\text{rel}} \approx \frac{0.1N}{\ln N} T_{\text{cross}} \approx 100 T_{\text{cross}}$ , such that two-body-encounter driven processes can be neglected during the simulations.

Before shifting to Milgromian gravity, we first virialise the models constructed from §2 in Newtonian gravity for  $\approx 25 T_{\text{cross}}^{\text{Newt}}$ , to fully phase mix the systems and test the stability of the unperturbed systems. The details of the stability test can be found in Appendix A. Then we evolve the systems in Milgromian gravity for another  $\approx 100 - 200$  Myr (200 Myr for models 3 and 5 to ensure there are more than  $10 T_{\text{cross}}^{\text{MD}}$  for each system) to study their re-virialisation process.

#### 3.2 Time scales

##### 3.2.1 Time scale of re-virialisation and the virial ratio

For a collisionless system, the scalar virial equation should be satisfied if the system is in equilibrium (Binney & Tremaine 2008):

$$2K + W = 0, \quad (5)$$

where  $K$  is the kinetic energy of the system and  $W$  is Clausius' integral,  $W = \int \rho \vec{x} \cdot \nabla \Phi d^3x$  (where  $\vec{x}$  is the spatial vector, Clausius 1870). Lynden-Bell (1967) showed that for a Newtonian system violently virialising to equilibrium, the time scale is approximately  $3T_r^*/8\pi \simeq T_r^*/8$ , where  $T_r^*$  is the typical radial period of the system at the equilibrium radius.  $T_r^*$  and  $T_{\text{cross}}$  should be of comparable magnitude. Therefore the violent virialisation time is comparable to a crossing time at the equilibrium radius. Nipoti et al. (2007) studied dissipationless collapses of systems in MD and they obtained a virialisation time  $\propto r(GMa_0)^{-1/4}$  for deep MD systems collapsing from rest (i.e. the initial velocities of the particle systems are zero). Since our systems evolve from one equilibrium state to another equilibrium state, the time scale for the re-virialisation should be comparable to this violent virialisation time scale in Milgromian gravity.

Fig. 2 shows the time scale of the re-virialisation of

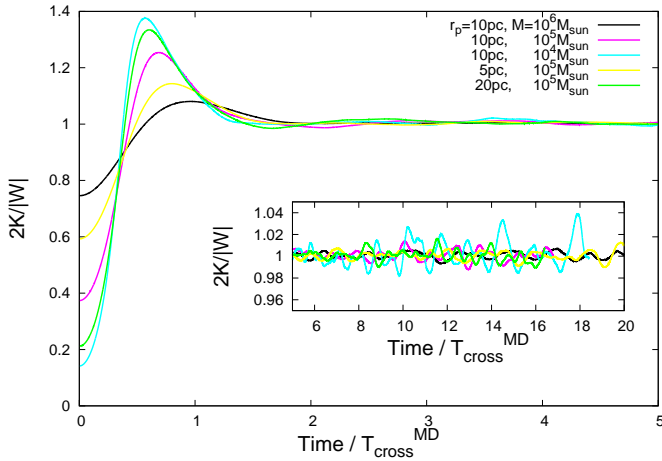


**Figure 2.** The virial ratio during the re-virialisation due to the phase transition. Time = 0 at the time when Newtonian gravity instantly transits into Milgromian gravity. After about 5 crossing times (see §3.2.1 for details) in Milgromian gravity, the systems are in their new equilibrium states.

the models. The virial ratios  $2K/|W|$  of all the models are smaller than 1 when the gravity is switched to Milgromian at Time = 0. The particles are accelerated in the deepened potential. We use the definition of a system’s ‘dynamical time’  $T_{\text{dyn}}$  in Nipoti et al. (2007), i.e. the time scale when  $2K/|W|$  reaches its maximum value.  $T_{\text{dyn}}$  is within  $0.5 - 1.0 T_{\text{cross}}^{\text{MD}}$ . The varying trend of the time scale for different models agrees with the violent re-virialisation time scale in Nipoti et al. (2007). The  $T_{\text{dyn}}$  of re-virialisation is approximately proportional to  $r_{\text{P}}(GMa_0)^{-1/4}$  here as well. We show the values of  $r_{\text{P}}(GMa_0)^{-1/4}$  in Table 1. We define the re-virialisation time to be  $5 \times T_{\text{dyn}}$ , since the amplitude of oscillation of  $2K/|W|$  around 1 is smaller than 1.5% at  $T > 5T_{\text{cross}}^{\text{MD}}$  in Fig. 2, and the systems can be considered fully re-virialised. From Fig. 2 we find that the time scale for the systems to re-virialise from Newtonian to Milgromian gravity is rather short, especially for the violent re-virialisation period.

### 3.2.2 Lagrangian radii, local time scales and mass profiles

We study the evolution of mass profiles of the models by considering their Lagrangian radii. We show one example (model 2) of the evolution of the 10% to 90% Lagrangian radii in Fig. 3. We define the ‘dynamical time of each 10% of mass shell’ (short for fractional dynamical time  $T_{\text{dyn}}^i$ ,  $i = 1, 2, \dots, 9$ ) as the time when its Lagrangian radius collapses to its minimal value. We find that the fractional dynamical time scales,  $T_{\text{dyn}}^i$ , are different for different enclosed mass: the time scale increases with increasing enclosed mass. The Lagrangian radii become smaller when re-virialised to Milgromian gravity especially for the inner regime. The  $T_{\text{dyn}}^i$  are important since they show the maximum time a regime can remain frozen in Newtonian gravity.

We show the fractional dynamical times  $T_{\text{dyn}}^i$  of all the models in the upper panel of Fig. 4. We find that  $T_{\text{dyn}}^i$  (in unit of  $1T_{\text{cross}}^{\text{MD}}$ ) as a function of the mass fraction is almost

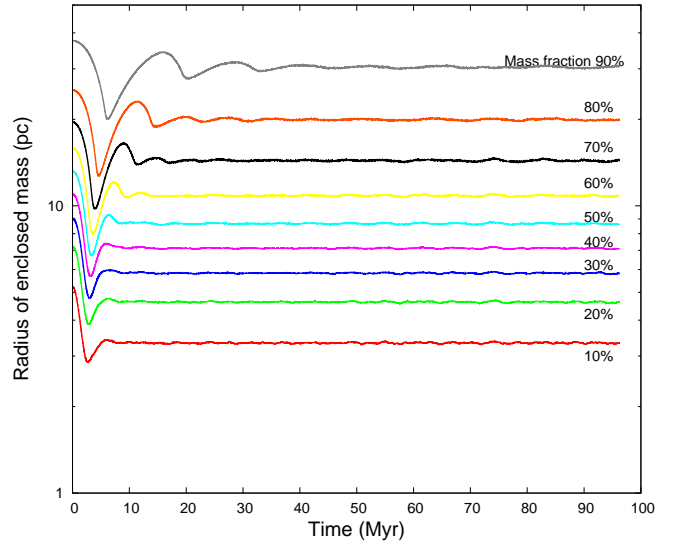


**Figure 3.** The evolution of the 10% – 90% Lagrangian radii for model 2. At Time = 0, Newtonian gravity switches instantly to Milgromian gravity.

the same for different models: from  $0.3 T_{\text{cross}}^{\text{MD}}$  to  $0.7 T_{\text{cross}}^{\text{MD}}$  for 10% – 90% of the enclosed mass. The innermost parts of the systems are frozen in Newtonian gravity for times shorter than  $0.3 T_{\text{cross}}^{\text{MD}}$ . The outermost parts of the systems are frozen for times shorter than  $0.7 T_{\text{cross}}^{\text{MD}}$ .

For each mass shell, the first oscillation from the initial value to the first maximum of the Lagrangian radius should be approximately a local crossing time. We call the time for the first oscillation of Lagrangian radii in each shell the ‘local transition time’,  $T_{\text{transition}}^i$ .  $T_{\text{transition}}^i$  versus mass fraction has the same trend as  $T_{\text{dyn}}^i$  in the upper panel. The local transition time scales are from  $0.4 T_{\text{cross}}^{\text{MD}}$  to  $1.1 T_{\text{cross}}^{\text{MD}}$  for 10% – 90% of the enclosed mass. However, there is a deviation of the local transition time curves between the different models normalised by their own  $1T_{\text{cross}}^{\text{MD}}$ : in the lower panel of Fig. 4, comparing models 1 (black curve), 2 (Magenta curve) and 3 (Cyan curve), the more massive models have longer time scales; and comparing models 2 (Magenta), 4 (Yellow) and 5 (Green), the models with smaller initial radii have longer time scales. I.e., the models with denser density distributions, where the gravity is stronger, have longer time scales in unit of  $T_{\text{cross}}^{\text{MD}}$ ; while the more diffuse models where their gravities are weaker, have shorter time scales in unit of  $T_{\text{cross}}^{\text{MD}}$ . This is because after  $T_{\text{dyn}}^i$ , the local particle structures over-collapse in Milgromian potential, and then oscillate back to the equilibrium state, and the diffuse models are closer to the deep MOND equilibrium after  $T_{\text{dyn}}^i$ .

The evolution of Lagrangian radii implies that the mass profiles of the GCs have changed after re-virialisation. We show the spherically averaged density profiles of the models in the upper panel of Fig. 7. The densities,  $\rho(r)$ , are normalised by  $\rho_0 = M/r_{\text{P}}^3$  so that all the Newtonian models stay on the same curve. In general the central densities become larger and the core radii are smaller after the re-virialisation. This agrees with the evolution of the Lagrangian radii. We further note that the diffuse models change their central density more than the compact models. This is because the

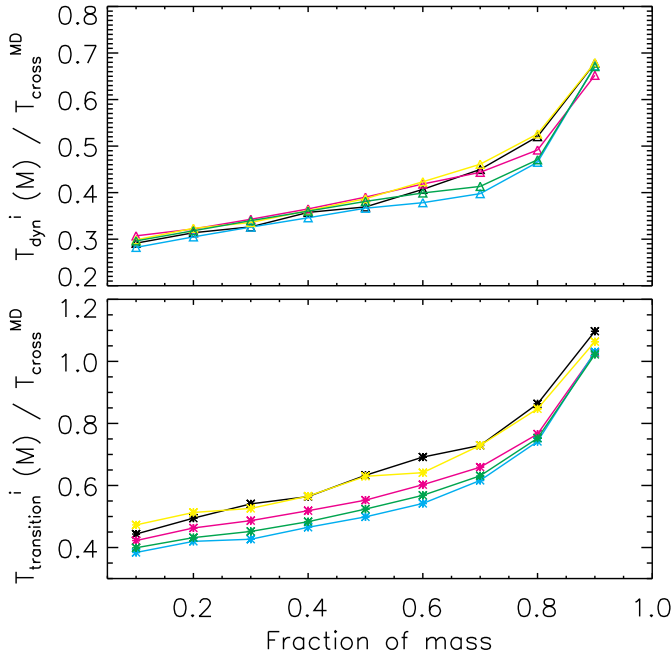


**Figure 4. Upper panel:** The time scale of the phase transition in units of the MD crossing time at the 10% – 90% Lagrangian radii. **Lower panel:**  $T_{\text{dyn}}^i$  at the 10% – 90% Lagrangian radii. The colours are for different models, as defined in Fig. 1.

more diffuse models are further away from equilibrium when the gravity switches from Newtonian to Milgromian.

### 3.2.3 Can Palomar 14-like GCs be frozen in Newtonian gravity?

There are distant GCs like Palomar 14 (hereafter Pal 14), which is located in a deep MD background (74.7 kpc distance to the Sun, Hilker 2006), but appear to behave Newtonian with a small value of the velocity dispersion (Haghi et al. 2009). This kind of GC seems to be a challenge to MD. However, Gentile et al. (2010) argued that Pal 14 is not sufficient enough to falsify MD, and one of their arguments is that Pal 14 could be on an eccentric orbit around the Milky Way, and that its potential is Newtonian at its pericentre due to the strong external field from the Milky Way: the Newtonian-like potential is frozen when Pal 14 moves to the current position. From Figures 2, 3 and 4 we find that the time scale of the transition is rather short and the systems go into the MD dominated regime in a few to a few tens of Myr. If the orbital time from the pericentre to the outer stellar halo of the Milky Way (i.e., far enough away where the external field is  $\ll a_0$ ) is shorter than the ‘dynamical’ time, it is possible that a GC may not be in equilibrium and its potential appears frozen in the Newtonian regime. We will briefly show the kinetics of rapid phase transition later in this section and show simulations for GCs moving on different radial orbits around the Milky Way in §4, for comparing the realistic time scale of re-virialisation and the orbital time.

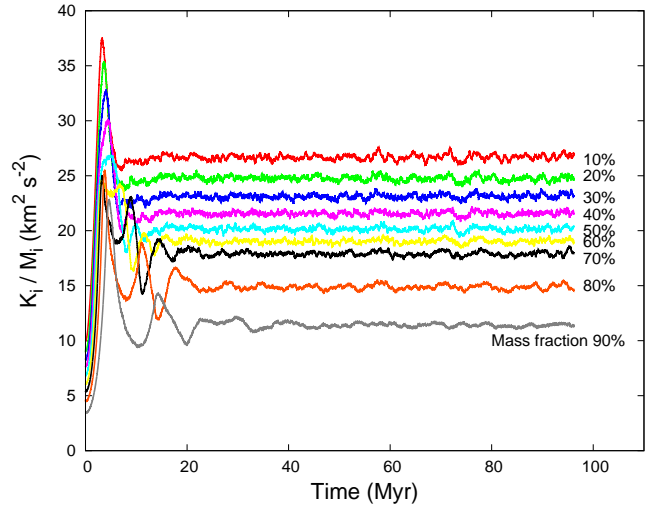


**Figure 5.** The evolution of the kinetic energy within shells of the 10% – 90% Lagrangian radii of model 2.  $M_i$  is the mass within the  $i_{th}$  equal mass shell. The Newtonian gravity switches instantly into Milgromian gravity at Time = 0.

### 3.3 Kinematics

For the particles in each shell of the 10% – 90% Lagrangian radii, the kinetic energy is defined as,

$$K_i = \frac{1}{2} \sum_{ip=1}^{N_{\text{parts},i}} m_{ip} v_{ip}^2, \quad (i = 1, 2, \dots, 9),$$

where  $N_{\text{parts},i}$  is the number of equal mass particles in the  $i_{th}$  shell and  $m_{ip}$  is the mass of  $ip_{th}$  particle. We show the evolution of  $K_i$  of model 2 in Fig. 5. The time scale of the first oscillation at different Lagrangian radii agrees with Fig. 3. Each shell is fully virialised after about  $5 T_{\text{dyn}}^i$ . The kinetic energy increases by a factor of 2.7 in the innermost shell and by a factor of 3.3 in the outermost shell for this model.

We also study the increment of  $K_i$  of all the models in Fig. 6, i.e.,  $\frac{K_{i, \text{re-virialised}}}{K_{i, \text{Newtonian}}}$  versus the fraction of mass. We find that the increasing curves of kinetic energy are mildly increasing with the fraction of mass for all the models, i.e., the kinetic energy in the inner parts of the systems increase slightly less than the increment of their outer parts. The trends of the curves for all the models are rather similar. There is a large oscillation for the cyan curve (i.e., model 3) since there are fewer particles in this model, and the particle noise is larger in this simulation.

The kinetic energies of the systems evolve significantly after the re-virialisation. Therefore the velocity dispersions should also evolve significantly. We study the radial velocity dispersion and the corresponding anisotropy profiles of the models before and after the re-virialisation. The middle panel of Fig. 7 shows the evolution of the  $\sigma_r(r_i)$  profiles:

$$\sigma_r^2(r_i) = \frac{1}{N_{\text{parts},i}} \sum_{ip=1}^{N_{\text{parts},i}} (v_{r,ip} - \bar{v}_{r,i})^2, \quad (6)$$

where  $r_i$  is the  $(i \times 10)\%$  Lagrangian radius,  $v_{r,ip}$  is the radial velocity of the  $ip_{th}$  particle and  $\bar{v}_{r,i}$  is the mean radial velocity of the particles in the  $i_{th}$  equal mass shell. The

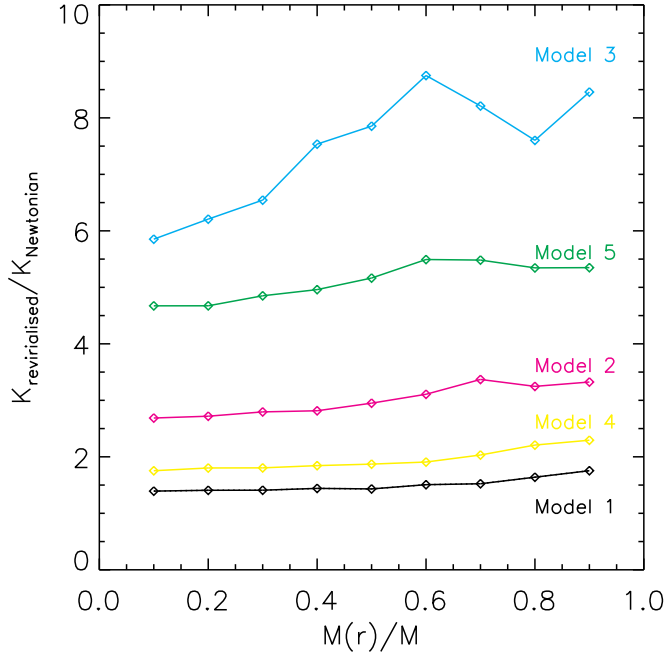


**Figure 6.** The increase of kinetic energy in each shell from Newtonian to Milgromian gravity. I.e.,  $\frac{K_{i, \text{re-virialised}}}{K_{i, \text{Newtonian}}}$ . The colours are for different models, as defined in Fig. 1.

original Newtonian models have decreasing  $\sigma_r(r_i)$  profiles (dotted curves) versus increasing radii  $r_i$ , while the final products can have decreasing profiles for the compact systems like models 1 (black) and 4 (yellow), or have  $\sigma_r(r_i)$  profiles that increase mildly at first and then decrease again in the outer regime for the loose systems like model 2. With a same mass (models 2, 4 and 5, i.e., magenta, yellow and green curves), the peak values of the increasing  $\sigma_r(r_i)$  profiles appear at a smaller mass fraction for the models with a larger initial Plummer radius  $r_P$ ; however the amplitudes of the  $\sigma_r(r_i)$  profiles do not change significantly with radius. This is different to the Newtonian case. The  $\sigma_r(r_i)$  profiles of self-consistent Newtonian models (the dotted curves) are very different if their  $r_P$  are different.

Since the systems collapse during the re-virialisation, the orbital structures might completely change. Nipoti et al. (2007) showed the anisotropy profiles of their rest models collapsing in Newtonian and Milgromian gravities, and their models become highly radially anisotropic after the virialisation, especially for their outer parts where  $r > 3r_h$  ( $r_h$  being the 3-dimensional half mass radius) for their deep Milgromian model, and  $r > r_h$  for mild-Milgromian and Newtonian models. Although our ICs are different to the ones in Nipoti et al. (2007), the re-virialisation from the Newtonian to the Milgromian regime is similar to the collapse process. We expect to obtain radially anisotropic models from our rapid phase transition as well. The anisotropy profiles  $\beta(r_i)$  are defined in the same way as that in Binney & Tremaine (2008),

$$\beta(r_i) \equiv 1 - \frac{\sigma_\theta^2(r_i) + \sigma_\phi^2(r_i)}{2\sigma_r^2(r_i)}, \quad (7)$$

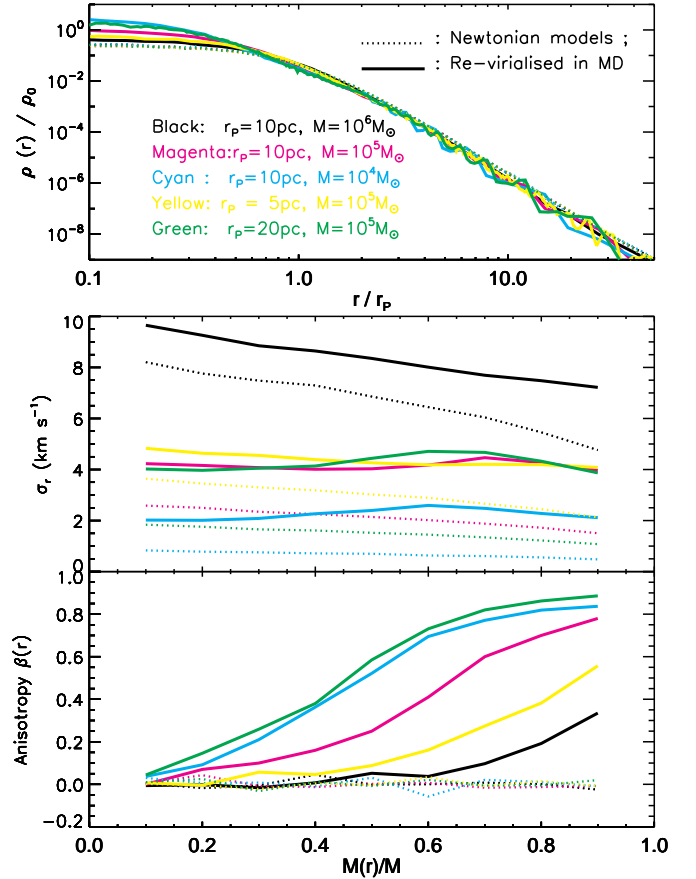


**Figure 7.** The spherically averaged density profiles (upper panel), radial velocity dispersion (middle panel) and anisotropy (lower panel, Eq. 7) for the models in Table 1. The dotted and solid lines correspond to, respectively, models in Newtonian and in Milgromian dynamics.

where  $\sigma_\theta$  and  $\sigma_\phi$  are polar and azimuthal components of velocity dispersion, and the definition is similar to that of radial velocity dispersion in Eq. 6. We show the  $\beta(r_i)$  profiles of our final products in the lower panel of Fig. 7. Indeed all of the  $\beta(r_i)$  profiles are radially anisotropic. The more compact models have larger anisotropic radii (i.e., the radii where the models start to be anisotropic) and they are less radially anisotropic, while the more diffuse systems have smaller anisotropic radii and they are more radially anisotropic. The  $\beta(r_i)$  profiles of model 3 and 5 are remarkably radial, they are almost linearly increasing from the 10% to the 60% enclosed mass radii and have  $\beta > 0.8$  at radii containing 60% of the enclosed mass, and then the  $\beta(r_i)$  profiles mildly increase with mass. Therefore diffuse models, whose self-gravity are in deep MD, change the anisotropy profiles more significantly than the compact models.

### 3.4 Phase space distribution during re-virialisation

In order to quantitatively compare the re-virialisation of systems from Newtonian to Milgromian dynamics with

Nipoti et al. (2007)’s dissipationless collapse process, the phase space distributions of the models are studied and three typical examples are shown in Fig. 8: models 4 (left panels), 2 (middle panels) and 5 (right panels), which represent systems in weak-, moderate- and deep-Milgromian dynamics, respectively. The phase space distributions are studied at times of  $0.5 T_{\text{cross}}^{\text{MD}}$ ,  $1 T_{\text{cross}}^{\text{MD}}$ ,  $17 T_{\text{cross}}^{\text{MD}}$  and  $35 T_{\text{cross}}^{\text{MD}}$ . The dynamical times for the majority parts of the systems are shown in Fig. 4, and  $1 T_{\text{dyn}}$  roughly amounts to  $0.7 T_{\text{cross}}^{\text{MD}}$  for the majority parts (90% enclosed mass) of the systems. Therefore,  $35 T_{\text{cross}}^{\text{MD}}$  roughly amounts to  $50 T_{\text{dyn}}$ . The times at which the phase space distributions are studied here are analogous to those in Nipoti et al. (2007,  $0.5 T_{\text{dyn}}$ ,  $1.0 T_{\text{dyn}}$ ,  $44 T_{\text{dyn}}$ ). Within  $35 T_{\text{cross}}^{\text{MD}}$  the systems are fully re- virialised, although in the very outer regimes there are few particles which have not yet phase mixed. We have to note that the amount of such particles are actually small and that there are only about 1.5% of mass outside a radius of  $10 r_p$ .

At the beginning of violent re- virialisation ( $0.5 T_{\text{cross}}^{\text{MD}}$  and  $1 T_{\text{cross}}^{\text{MD}}$ ), particles fall into the centres of the systems, and some of the particles have already crossed the centres, which correspond to the particles near  $r = 0$ . This is similar to that of dissipationless collapse. However, the phase space distributions have wider spreads compared to that at the beginning of dissipationless collapse (Nipoti et al. 2007). The reason is that the phase transitions of our models start from Newtonian equilibrium state, while the dissipationless collapse processes start from rest. At time  $T = 1.0 T_{\text{cross}}^{\text{MD}}$ , the deeper the Milgromian dynamics dominating the systems is, the clearer the shell-like structures appear near the centre of the systems. Those shell-like structures are particles moving in and out of the systems in the centre regimes. Before the systems are phase mixed, the shell-like structures will appear in the outer regimes of the systems as time is proceeding. At  $T = 17 T_{\text{cross}}^{\text{MD}}$ , the weak-Milgromian system has already erased all structures. This implies that it approaches a phase mixed state. However, the other two models still have shell-like structures outside  $3 r_p$ , especially for the deep-Milgromian system. This is similar to the case of dissipationless collapse since the Milgromian system is less efficient in phase mixing. The enclosed mass within  $3 r_p$  is 85.4% of the overall mass. Therefore, the regimes which contain shell-like structures at  $T = 17 T_{\text{cross}}^{\text{MD}}$  are the outer regimes of the systems. We further evolve the systems 2 and 5 until  $T = 35 T_{\text{cross}}^{\text{MD}}$ , and then compare with model 4. After  $35 T_{\text{cross}}^{\text{MD}}$  the shell-like structures of all the models disappear, which means the models are fully phase mixed. The phase mixing process in the re- virialisation case is shorter than that in the dissipationless collapse process (Nipoti et al. 2007).

### 3.5 Radial Instability after systems re- virialised

From the studies of §3.3, one can see that the diffuse systems going into the deep-Milgromian dynamics regime (Models 3 and 5) are strongly radially anisotropic from the half-mass radii outwards. There are many radial orbits in the deep-Milgromian systems after re- virialisation. Since the re- virialisation of the systems is a new prediction compared to Newtonian dynamics, it is important to examine whether the re- virialised systems are stable, i.e., whether their velocity dispersions become isotropic by the effect of radial

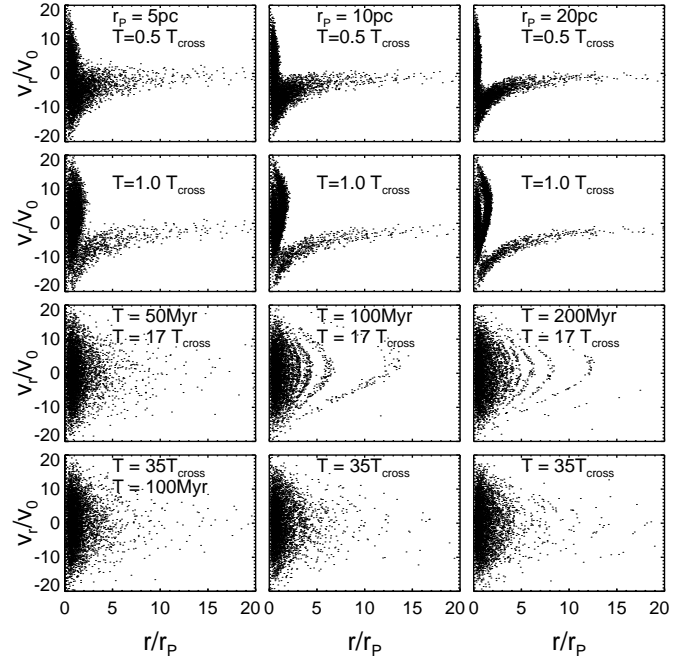


**Figure 8.** The phase space distribution at different snapshots of violent re- virialisation for models 4 (left panels), 2 (middle panels) and 5 (right panels). The radii are scaled by the initial Plummer radius  $r_p$ , and the radial velocities of particles,  $v_r$ , are scaled by  $v_0 = \sqrt{GM/r_p}$ .

instability. A parameter describing the ratio between radial and tangential anisotropies was defined in Trenti & Bertin (2006); Polyachenko & Shukhman (1981),

$$\xi = \frac{2K_r}{K_t}, \quad (8)$$

for a globe (Newtonian) system, to characterize the stability of the system. Here  $K_r$  and  $K_t = K_\theta + K_\phi$  are the radial and tangential components of the kinetic energy tensor, respectively.  $K_r \equiv \sum_{ip=1}^N \frac{1}{2} m_{ip} v_{r,ip}^2$ , where  $N$  is the total number of particles for a system. The polar and azimuthal components of the kinematic energy tensor, represented by  $K_\theta$  and  $K_\phi$  respectively, can be defined in the same manner. Nipoti et al. (2011) applied the  $\xi$  parameter for Milgromian systems, and found that there is an empirical stability criterion for Milgromian systems:  $2.3 \leq \xi_c \leq 2.6$  for the stellar components, where the  $\xi_c$  is the critical value of  $\xi$  which depends on the stellar density and internal gravitational acceleration. The systems are stable if  $\xi \leq \xi_c$ . The  $\xi$  values for the models after re- virialisation are listed in the 8<sup>th</sup> column of Table 1. The values of  $\xi$  for models 1, 2, 3 and 4 are smaller than 2.3, and  $\xi$  for model 5 is 2.37, which is within the range of  $\xi_c$ . Therefore models 1 – 4 are stable models, and model 5 is at the critical limit.

## 4 GLOBULARS IN THE SPACE-VARYING GRAVITATIONAL FIELD OF THE GALAXY

We have already studied the violent re- virialisation in §3, and we showed that the re- virialisation takes only a few crossing times in Milgromian gravity, which is too short to

freeze the distant GCs in Newtonian gravity. However a real star cluster moving in the Galactic potential experiences gradually evolving dynamics. The self-gravity of an equilibrium system moving in such a field is gradually evolving, and the transition between (quasi-) Newtonian and Milgromian gravity may be adiabatic. Thus an adiabatic contraction or expansion process is expected for such a system. However this has not yet been studied for a system moving in a gravitational background field which is continuously space-varying.

Here we are interested in the adiabatic contraction process since it is a brand new physical process. We will select and virialise the Newtonian systems from §2 in a strong external field from the Milky Way in §4.2, and then send the systems on different radial orbits along the vertical  $z$ -axis of the Milky Way in §4.3. We shall compare the time scale of the phase transition, the kinematics and mass profiles of the final systems in §4.4.

#### 4.1 Background gravitational fields from the MW

The internal dynamics of a system embedded in an external field has been studied by Zhao & Tian (2006) and Wu et al. (2007). The Poisson equation of this system is linearised in the radii where the system is dominated by the external field. Assuming the external field is along the  $z$ -axis and using  $(x, y, z)$  Cartesian coordinates,

$$\Phi_{\text{int}}^{\infty}(x, y, z) = -\frac{GM}{\mu_e \sqrt{(1 + \Delta_e)(x^2 + y^2) + z^2}}, \quad (9)$$

where  $\Phi_{\text{int}}^{\infty}$  is the internal potential at infinity (i.e., at radii of the internal system where the self-gravity  $\mathbf{g}_{\text{int}}$  is much smaller than  $\mathbf{g}_{\text{ext}}$ , we can ignore  $\mathbf{g}_{\text{int}}$  in Eq. 1),  $\mu_e$  is the  $\mu$  function of the external field  $\mathbf{g}_{\text{ext}}$ , and  $\Delta_e \equiv \frac{d \ln \mu_e}{d \ln X_e} |_{X_e = |\mathbf{g}_{\text{ext}}|/a_0}$ .

Another important issue is the tidal field of the background. In Zhao & Tian (2006) the tidal radii of binary systems in MD-like gravity have been studied,

$$r_{\text{tidal}} = \left[ \frac{M_{\text{int}}}{(1 + \zeta)M_{\text{ext}}} \right]^{\frac{1}{3}} D_0, \quad (10)$$

where  $D_0$  is the orbital distance of the internal system,  $M_{\text{int}}$  is the total mass of the internal system and  $M_{\text{ext}}$  is the mass of the external system enclosed within the radius  $D_0$ ,  $\zeta = -\frac{d \ln g_{\text{int}}}{d \ln D_0} = 1 - \frac{d \ln v_{\text{cir}}^2}{d \ln D_0}$ , where  $\zeta = 1$  in deep MD gravity and  $\zeta = 2$  in Keplerian (or Newtonian) gravity, and  $v_{\text{cir}}$  is the circular velocity at the radius  $D_0$ . For radii  $r < r_{\text{tidal}}$  of the internal system, the tidal field is not important, and the background field is dominated by a homogeneous external field. A numerically homogeneous external field can be added as a boundary condition while solving the Poisson equation (Wu et al. 2007, 2008). The same boundary conditions were introduced into NMODY in Wu et al. (2010).

Since Plummer profiles are extended density profiles, it is impossible and unnecessary to study 100% of the enclosed mass. We define the inner 90% of the total mass as the majority of the system. We only focus on the dynamics of the inner 90% of the system, i.e., for  $r \simeq 3.7 r_{\text{P}}$ . Therefore only if  $r_{\text{tidal}} > 3.7 r_{\text{P}}$ , the homogeneous boundary condition can be applied.

We shall model GCs moving in the Milky Way's

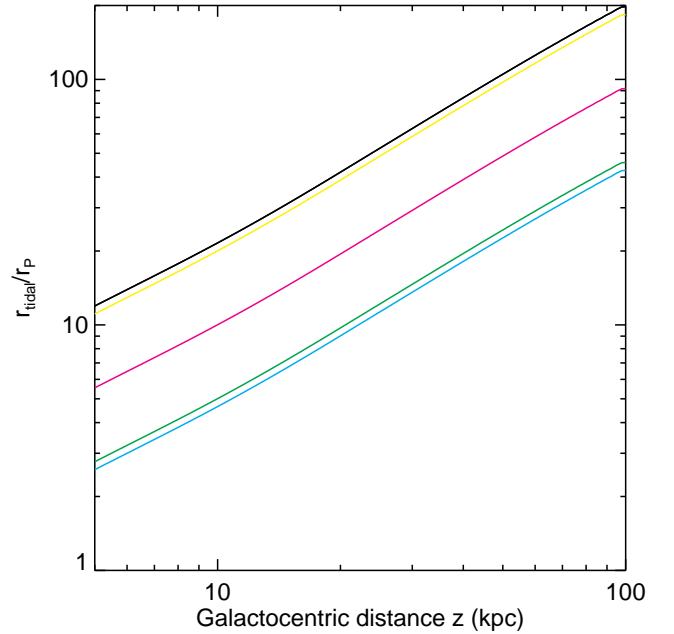


**Figure 9.** The tidal radii of the models from Table 1 at different Galactocentric distances. The Milgromian Besançon Milky Way potential is used here. The colours for different models are the same as defined in Fig. 1.

potential. The Milgromian Besançon Milky Way model (Robin et al. 2003) is studied by Wu et al. (2007, 2008) and Bienaymé et al. (2009), in which the dark matter halo is removed and Milgromian dynamics is applied. We reproduce the Milky Way's Milgromian potential and gravity with the Besançon density profile (Robin et al. 2003; Wu et al. 2007, 2008) in this work, using the code called NMODY (Londrillo & Nipoti 2009), with a resolution of  $n_r^{\text{MW}} \times n_\theta^{\text{MW}} \times n_\phi^{\text{MW}} = 500 \times 64 \times 128$  using spherical coordinates  $(r, \theta, \phi)$ . The method of grid segmentation is the same as in §3.1, and  $r_s^{\text{MW}} = 10.0$  kpc. The angular resolution of the spherical harmonic expansion is  $l_{\text{max}}^{\text{MW}} = 16$ . There is a weak external field of  $0.01 a_0$  applied to the MW in the direction Sun-Galactic centre, which comes from the combination of the local gravitational attractors, i.e., the Great Attractor (see Radburn-Smith et al. 2006), the M31 galaxy, the Coma and Virgo clusters (more details of the modelling of the Galaxy are in Wu et al. 2007, 2008).

We will move the systems along the vertical  $z$ -axis of the MW. We calculate the tidal radii of the models from Tab. 1 at different Galactocentric distances, from 5 kpc to 100 kpc. The background field of the MW at the position  $(x, y, z) = (0, 0, 5)$  kpc is  $\approx 2.1 a_0$ , which is strong enough to reduce the Milgromian effect, and the dynamics of a GC embedded in this external field is Newtonian-like. We show the tidal radii in Fig. 9. Note that the tidal radii of models 3 and 5 (cyan and green curves) are only  $\approx 2.5 r_{\text{P}}$  when they are placed at the position  $(x, y, z) = (0, 0, 5)$  kpc. Therefore models 3 and 5 are not suitable to use the homogeneous boundary condition in Eq. 9. Theoretically we can choose a larger Galactocentric distance, say  $z = 10$  kpc, as starting points of the moving orbits for models 3 and 5. However the

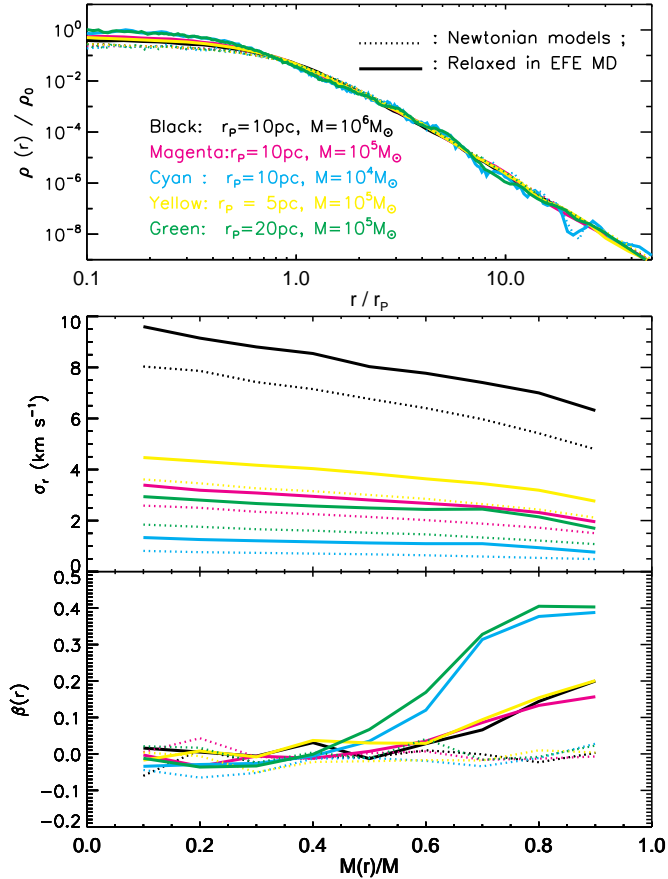


**Figure 10.** The spherically averaged density (upper panel), radial velocity dispersion (middle panel) and anisotropic profiles (lower panel, Eq. 7) for models 1 (black), 2 (magenta) and 4 (yellow) before (dotted curves) and after (solid) virialisation in strong Galactic fields. The models 3 (cyan) and 5 (green) are overplotted as comparison.

background field from the MW at  $(x, y, z) = (0, 0, 10)$  kpc is also weaker,  $\approx 1.0a_0$ . The Milgromian effects are remarkable for models 3 and 5 in such an external field. Therefore models 1, 2 and 4 in Table 1 are more interesting.<sup>1</sup>

#### 4.2 ICs in quasi-Newtonian dynamics

At the Galatocentric position of  $(x, y, z) = (0, 0, 5)$  kpc, the external field from the MW is strong. Therefore GCs staying at this position are dominated by quasi-Newtonian dynamics, i.e.,  $\mu(X) = \mu\left(\frac{|\mathbf{g}_{\text{ext}}| + |\mathbf{g}_{\text{int}}|}{a_0}\right) \approx 1$  in Eq. 1. The boundary conditions of the Poisson equation follow Eq. 9. The differences to Newtonian dynamics are: there is a constant factor of  $1/\mu_e$  on depth of the potential and a dilation factor of  $(1 + \Delta_e)$  on the shape of the potential. Therefore the quasi-Newtonian potential is  $(1/\mu_e - 1)$  deeper and it is

<sup>1</sup> For comparison, we will also show the re-virialisation of models 3 and 5 at  $(x, y, z) = (0, 0, 10)$  kpc and then will move them on radial Galactic orbits.

prolate. Thus it is necessary to virialise the systems in the quasi-Newtonian potentials first, to ensure the equilibrium of the systems.

We virialise the models of interest in the background field of  $\mathbf{g}_{\text{ext}} = (0, 0, 2.1a_0)$  for about 100 Myr. We show the density, radial velocity dispersion and anisotropy profiles in Fig. 10. We find that after the virialisation, the density profiles do not change significantly, however the inner regime of the GCs become denser, by a factor of 1 – 3. The radial velocity dispersion profiles are systematically shifted, with a 20% increment. The shape of the velocity dispersion profiles do not change after the virialisation. The change of density and radial velocity dispersion are due to the deepening of the potential. We also find that the isotropic models become slightly radially anisotropic after the virialisation (the lower panel). The systems become radially anisotropic from the half mass radii of the systems outwards and the anisotropies reach up to 0.2 at the radii where 90% of the mass is enclosed. The radial anisotropies come from the asymmetric internal potential due to the homogeneous external field effect (Wu et al. 2010): at the radii where the internal and external fields are comparable, the potentials of the internal systems are lopsided. The lopsidedness of the potential changes the orbits in the systems. This is quite similar to the radial anisotropy induced by tidal fields at an early stage in Newtonian dynamics. There are already many contributions on the dynamical evolution of star clusters in tidal fields in Newtonian gravity (Giersz & Heggie 1997; Takahashi & Lee 2000; Baumgardt & Makino 2003; Lee et al. 2006). In Newtonian dynamics, the tidal fields will bring in a strongly radial anisotropy in the outer regimes of the star clusters at an early stage, whereas the star clusters are still isotropic in the inner regimes (Takahashi & Lee 2000). The radial anisotropy in the outer parts disappears quickly with time in realistic tidal fields (Baumgardt & Makino 2003). Finally, the outer regimes of star clusters in Newtonian tidal fields become tangentially anisotropic (Giersz & Heggie 1997; Lee et al. 2006).

We have to note that this is not a tidal effect in MD, but an EFE which plays a similar role. The tidal radii (Eq. 10) are much larger than the radii at which EFE becomes important. Comparing Fig. 10 with Fig. 7, we find that the anisotropy introduced by the EFE is milder than by the phase transition. However for the most compact system, model 1, the anisotropy introduced by the two effects are comparable. This is because model 1 is so compact that it is mostly dominated by Newtonian dynamics, and it does not evolve as much as the other more diffuse models during the phase transition.

In Fig. 10 we also virialise models 3 and 5 in the background field at the Galactic position of  $(x, y, z) = (0, 0, 10)$  kpc for comparison. The external field is as strong as  $1.0 a_0$ . We overplotted the revirialised initial Newtonian models in this Milgromian external field (cyan and green curves in Fig. 10). We find that the density profiles and anisotropy profiles of models 3 and 5 change more compared to the other models: The centre densities are more concentrated and the anisotropy in the outer regimes is more radial for models 3 and 5, since at  $(x, y, z) = (0, 0, 10)$  kpc the Galactic field is weaker and the deviation from Newtonian dynamics becomes important. With a Galactic gravitational

field of  $1.0 a_0$ , the Newtonian and Milgromian accelerations are comparable.

### 4.3 Radial orbits of GCs

The models are fully virialised for about 100 Myr in the strong field in Milgromian gravity (when  $a \gg a_0$  this becomes identical to Newtonian gravity). We shall move the virialised models (1, 2 and 4) in the Galactic potential from near the Galactic centre, i.e., from a position at  $(x, y, z) = (0, 0, 5)$  kpc. The external field changes fastest along the polar direction on a pure radial orbit for a given initial velocity. Besides, the major part of a system should be enclosed within its tidal radius, so we need to avoid GCs moving near the Galactic disc plane. Therefore we choose orbits along the polar direction and there are only non-zero values of the initial velocity along the  $z$ -axis.

We setup a grid resolution of  $n_r^{\text{GC}} \times n_\theta^{\text{GC}} \times n_\phi^{\text{GC}} = 100 \times 32 \times 64$ , where the radial scaling parameter  $r_s^{\text{GC}} = 20$  pc and  $l_{\text{max}}^{\text{GC}} = 6$  since the GC models are spherically symmetric. The time steps are defined as in §3.1. In each simulation, we solve the Poisson equation for the Milky Way and store the gravitational acceleration field and potential on the grid, and then we interpolate the Galactic acceleration field and potential to the point where the centre of mass (CoM) of the GC is. Applying the boundary conditions of Eq. 9 onto the GC, the Poisson equation for the GC is computed. The positions and velocities of particles of the GC are updated each time step by the Leap-frog scheme, as in §3.1. The new CoM of the GC is calculated at the end of the time step, and then the external field of the new CoM of the GC is interpolated from the MW acceleration field and potential. At each time step of the GC, the EF is updated from the CoM position, such that the GC is embedded in a space-varying external field.

We choose a range of initial velocities  $v_z = 200 \text{ km s}^{-1}$ ,  $300 \text{ km s}^{-1}$ ,  $400 \text{ km s}^{-1}$ ,  $500 \text{ km s}^{-1}$ ,  $600 \text{ km s}^{-1}$ , to move the GCs from the quasi-Newtonian regime to the Milgromian regime in the Galactic background field on different time scales. We show the orbits in Fig. 11. We find that orbits with an initial velocity of  $200 \text{ km s}^{-1}$  and  $300 \text{ km s}^{-1}$  reach their apocentres at small radii, at about 8 kpc and 18 kpc respectively, and they cannot propagate to the outer part of the Galaxy. Thus these orbits are not of our interest. The dynamics of GCs moving on orbits with  $v_z = 400 \text{ km s}^{-1}$ ,  $500 \text{ km s}^{-1}$ ,  $600 \text{ km s}^{-1}$  are studied in §4.4. We move the GCs on these orbits for  $\approx 500$  Myr, which is long enough for the GCs to move to their apocentres or to the outer Galactic regime ( $r \approx 90$  kpc) where the distant Galactic GCs are observed (Baumgardt et al. 2005; Bellazzini 2007). We point out that the apocentre for the orbits with  $v_z = 400 \text{ km s}^{-1}$  is about 72 kpc. We study the kinematics of the GCs at their apocentres or at Galatocentric distance of 90 kpc, if their apocentres are even more distant. The orbital times from the initial position to the apocentre or to  $z = 90$  kpc are: 360 Myr for  $v_z = 400 \text{ km s}^{-1}$ , 270 Myr for  $v_z = 500 \text{ km s}^{-1}$  and 180 Myr for  $v_z = 600 \text{ km s}^{-1}$ . We note that the orbital time to transform the external field from the strong to the weak field is much longer than the re-virialisation time of  $5 \times T_{\text{dyn}}$ , therefore the GCs are re-virialised gradually in

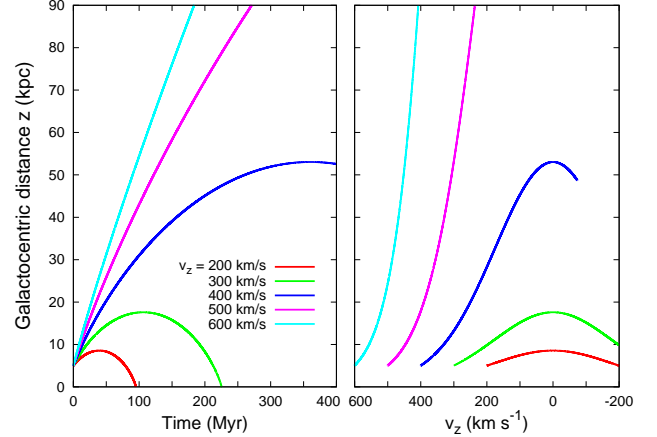


**Figure 11.** The radial orbits with different initial velocities starting from the position of  $(x, y, z) = (0, 0, 5)$  kpc. **Left panel:** Galatocentric distances versus orbital time. **Right panel:** Galatocentric distances versus radial velocity.

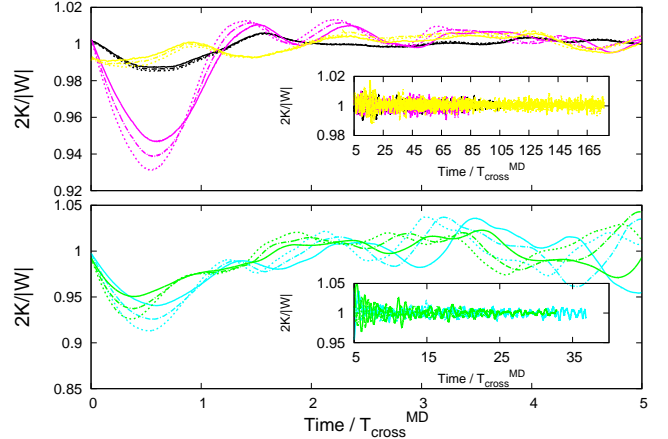


**Figure 12.** Upper panel: The virial ratio of models 1 (black), 2 (magenta) and 4 (yellow) moving on radial orbits in the MW potential, with initial velocities of  $400 \text{ km s}^{-1}$  (solid),  $500 \text{ km s}^{-1}$  (dot-dashed) and  $600 \text{ km s}^{-1}$  (dashed). Lower panel: The virial ratio of models 3 (cyan) and 5 (green) for comparison. The values of  $T_{\text{cross}}^{\text{MD}}$  can be found from Table 1.

the slow-evolving gravitational field. The phase transitions are adiabatic.

For models 3 and 5, the starting points of the Galactic orbits are  $(x, y, z) = (0, 0, 10)$  kpc, and the models are moving on the same Galactic orbits as models 1, 2 and 5. The initial velocities are interpolated at the starting point from the above Galactic orbits (see Fig. 11).

## 4.4 Adiabatically evolving systems

### 4.4.1 Virial ratios

The upper panel of Fig. 12 shows the virial ratios of the GCs moving on the different orbits. We find that the systems are not violently re-virialised compared to the case of the rapid

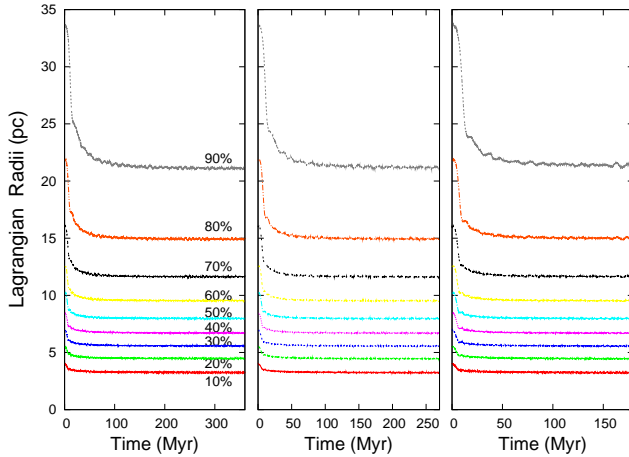


**Figure 13.** The evolution of Lagrangian radii of model 2 on different Galactic orbits starting from  $(x, y, z) = (0, 0, 5)$  kpc and ending at their apocentres or at  $r^{\text{MW}} = 90$  kpc if the apocentres are even further away (see Fig. 11), with different initial velocities:  $v_z = 400 \text{ km s}^{-1}$  (left panel),  $500 \text{ km s}^{-1}$  (middle panel),  $v_z = 600 \text{ km s}^{-1}$  (right panel).

phase transition. The virial ratios only deviate by 7% from 1 at most within the first 5 crossing times. For the compact models 1 and 4, the deviation is within 1% in the first 5 crossing times. Since the external fields are evolving, there is a noise of 1.5% at  $T \approx 18 T_{\text{cross}}^{\text{MD}}$ . Thereafter the fluctuations of virial ratios are within 1% around 1. Therefore the systems are only slightly out of virial equilibrium at the beginning of a Galactic orbit, where they are close to the Galactic centre and the gravitational field changes fastest. As we see from Fig. 12, from  $5 T_{\text{cross}}^{\text{MD}}$  onwards the systems are in equilibrium since the external field changes gradually. The differences of the time scales for systems reaching equilibrium states caused by different initial velocities can be ignored. Thus systems evolve adiabatically and the collapse process is much more moderate. The systems are very unlikely to be frozen in Newtonian dynamics when they move into the Milgromian regime, even when they are on an orbit with a high initial out-going velocity of as high as  $600 \text{ km s}^{-1}$ .

The virial ratio of models 3 and 5 are shown in the lower panel of Fig. 12. The amplitudes of the deviations to virial equilibrium are about 7%, which is much smaller than that of the violent re-virialisation. The virial ratios oscillate around 1 with a larger noise, since models 3 and 5 are originally further away from virial equilibrium at their initial Galactic position of  $(x, y, z) = (0, 0, 10)$  kpc. And the time scale of their phase transition is very similar to the cases of models 1, 2 and 4: from  $7 T_{\text{cross}}^{\text{MD}}$  onwards the systems are in virial equilibrium. It confirms again that the freezing time scales in quasi-Newtonian dynamics are only a few  $T_{\text{cross}}^{\text{MD}}$ , and the dynamics of the models quickly becomes Milgromian on their radial Galactic orbits.

#### 4.4.2 Lagrangian radii and mass profiles

We show the evolution of Lagrangian radii of model 2 in Fig. 13. The three panels correspond to different initial velocities of the Galactic orbits:  $v_z = 400 \text{ km s}^{-1}$  (left panel),

$500 \text{ km s}^{-1}$  (middle panel) and  $600 \text{ km s}^{-1}$  (right panel). The GC moves from the Galactic position of  $(x, y, z) = (0, 0, 5)$  kpc to the apocentre of the orbit (for the orbit of  $v_z = 400 \text{ km s}^{-1}$ ) or to  $r^{\text{MW}} = 90$  kpc where the most distant GC is observed. Compared to Fig. 3, we find that the adiabatic evolution is significantly different to the violent evolution: the Lagrangian radii decrease fast during the first  $\approx 20 T_{\text{dyn}}^i$  (see Fig. 4), and then the Lagrangian radii are almost constant, with tiny oscillations. There are no significant oscillation of the radii within the first  $20 T_{\text{dyn}}^i$ . This agrees with the evolution of virial ratios in Fig. 12. We also find that the final stable Lagrangian radii of the same fraction of enclosed mass do not change with different Galactic orbits. I.e., models 2 moving on different radial orbits have the same Lagrangian radii when they are in the outer regime of the Galaxy. This implies that a GC in the outer regime of the MW will have a universal mass profile, which does not depend on the Galactic orbit. The evolution of Lagrangian radii of the other models are similar to that of model 2.

We study the mass profiles of the GCs embedded in a strong field and in weak fields (at the apocentres of different orbits, or at  $r^{\text{MW}} = 90$  kpc) in the upper panel of Fig. 14. We find that the densities of the GCs after adiabatic compression are very similar to the case of violent collapse: The densities in the core regime become larger while in the outer regime at  $r > 3r_p$  they are smaller. For a same model, the final density profiles for different Galactic orbits are very similar.

We also study the axis-ratios of the 50% and 90% enclosed mass of the initial GCs at a Galatocentric position of  $(0, 0, 5)$  kpc and of the final products (GCs at large radii of the Galaxy). The axis-ratios are defined as  $a : b : c = \sqrt{I_{xx}} : \sqrt{I_{yy}} : \sqrt{I_{zz}}$ , where the  $I_{xx}$ ,  $I_{yy}$  and  $I_{zz}$  are the diagonalised moments of inertia tensor directions (Gerhard 1983):

$$\begin{aligned} I_{xx} &= \frac{1}{N_{\text{parts}}} \sum_{\text{ip}=1}^{N_{\text{parts}}} \frac{(y_{\text{ip}}^2 + z_{\text{ip}}^2)}{r_{\text{ip}}^2}, \\ I_{yy} &= \frac{1}{N_{\text{parts}}} \sum_{\text{ip}=1}^{N_{\text{parts}}} \frac{(x_{\text{ip}}^2 + z_{\text{ip}}^2)}{r_{\text{ip}}^2}, \\ I_{zz} &= \frac{1}{N_{\text{parts}}} \sum_{\text{ip}=1}^{N_{\text{parts}}} \frac{(x_{\text{ip}}^2 + y_{\text{ip}}^2)}{r_{\text{ip}}^2}, \end{aligned} \quad (11)$$

where  $r_{\text{ip}} = \sqrt{x_{\text{ip}}^2 + y_{\text{ip}}^2 + z_{\text{ip}}^2}$ , and  $N_{\text{parts}}$  is the enclosed number of particles in the ellipsoids of  $\left(\frac{x}{a}\right)^2 + \left(\frac{y}{b}\right)^2 + \left(\frac{z}{c}\right)^2 = r_{50}^2$  (or  $= r_{90}^2$ ), where  $r_{50}$  and  $r_{90}$  are the radii enclosing 50% and 90% of mass, respectively. The axes of the GCs are listed in Table 2. When the models are at their starting points of the orbits, they are embedded in a strong external field, therefore the internal potentials of the GCs are prolate, especially for the outer parts (Wu et al. 2007, 2008). This is even more significant in models 3 and 5, since their internal structures are more diffuse than the other models.

We find that at their half mass radii (i.e.,  $r_{50}$ ), the models are slightly prolate since they are dominated by their internal fields at  $r_{50}$ . At the radii of  $r_{90}$ , the deviation from a spherical shape is larger, for model 2 the axis-ratio is  $1 : 0.94 : 0.94$ . The GCs at the end of their out-going orbits are very close to be spherically symmetric after the compres-

**Table 2.** Axis-ratios of the mass distribution of the GCs: The first column shows the ID of the models in Tab 1, the second column shows the axis-ratios (see Eq. 11) of the GCs at  $T = 0$  near the Galactic plane, at the Galatocentric position  $(0, 0, 5)$  kpc for models 1, 2 and 4, and  $(0, 0, 10)$  kpc for models 3 and 5. The third to the fifth columns show the axis-ratios of the GCs in the outer regime of the Milky Way. The two parts of the table show the axis-ratios within  $r_{50}$  (first three lines) and  $r_{90}$  (last three lines).

Models	Inner MW	Apocentre $v_z = 400 \text{ km s}^{-1}$	$r^{\text{MW}} = 90 \text{ kpc}$ $v_z = 500 \text{ km s}^{-1}$	$r^{\text{MW}} = 90 \text{ kpc}$ $v_z = 600 \text{ km s}^{-1}$
$(a : b : c)_{r_{50}}$				
1	1 : 0.98 : 0.99	1 : 0.99 : 0.99	1 : 0.99 : 0.98	1 : 0.99 : 0.99
2	1 : 0.98 : 0.97	1 : 0.99 : 0.99	1 : 1.00 : 0.99	1 : 1.01 : 1.01
3	1 : 0.96 : 0.95	1 : 0.93 : 0.92	1 : 0.97 : 0.96	1 : 0.96 : 0.97
4	1 : 0.97 : 0.96	1 : 0.99 : 0.99	1 : 1.00 : 0.99	1 : 0.99 : 0.99
5	1 : 0.95 : 0.95	1 : 0.96 : 0.96	1 : 0.98 : 0.97	1 : 0.97 : 0.96
$(a : b : c)_{r_{90}}$				
1	1 : 0.98 : 0.97	1 : 0.99 : 0.99	1 : 0.99 : 0.99	1 : 0.99 : 0.99
2	1 : 0.94 : 0.94	1 : 0.97 : 0.98	1 : 0.99 : 0.99	1 : 0.99 : 0.99
3	1 : 0.88 : 0.88	1 : 0.88 : 0.89	1 : 0.92 : 0.92	1 : 0.91 : 0.92
4	1 : 0.95 : 0.95	1 : 0.99 : 0.99	1 : 0.99 : 0.99	1 : 0.99 : 0.99
5	1 : 0.89 : 0.89	1 : 0.92 : 0.92	1 : 0.94 : 0.94	1 : 0.93 : 0.94

sion process. There is only a deviation from a sphere of 1% in both the inner and the outer parts of most of the models and for all radial orbits. For the moderately diffuse system, model 2 on an orbit with  $v_z = 400 \text{ km s}^{-1}$ , the axis-ratios at  $r_{90}$  are slightly prolate, 1 : 0.97 : 0.98. This is because model 2 is more diffuse compared to the models 1 and 4, and at the radius of  $r_{90}$  and the apocentre of the Galactic orbit, the external field can affect the outer parts. While model 2 moves further away, say to  $r^{\text{MW}} = 90 \text{ kpc}$ , the external field is weaker than at the apocentre of the first Galactic orbit, and the model becomes spherically symmetric again.

Models 3 and 5 confirm this trend: they are intrinsically even more diffuse than model 2, therefore they are even more prolate at both  $r_{50}$  and  $r_{90}$ . However, the deviations from spherical symmetry are next to negligible for all models.

#### 4.4.3 Velocity dispersion and anisotropy

The radial velocity dispersion profiles are studied in the middle panel of Fig. 14. The shapes of the final radial velocity dispersion profiles are very similar to those of the violent re-virialisation. However, there are small differences between the profiles for GCs collapsing violently and adiabatically, especially for the diffuse GCs, model 2, and also the most diffuse models 3 and 5. Compared to the middle panel of Fig. 7, models 2, 3 and 5 have increasing and then decreasing profiles in the intermediate regime between  $r_{50}$  (where  $\frac{M(r)}{M} = 0.5$ ) and  $r_{90}$  (where  $\frac{M(r)}{M} = 0.9$ ) for the violent collapse cases, while the  $\sigma_r(r)$  profiles are almost flat for the case of adiabatic collapse. In the other two models the  $\sigma_r(r)$  profiles are almost the same for adiabatic and violent collapses. Moreover, we find that the  $\sigma_r(r)$  profiles of the final products are independent of their Galactic orbits. Different Galactic orbits lead to a similar  $\sigma_r(r)$  profile when the GCs are in the outer regime of the Galaxy.

There are more differences in the anisotropy profiles when comparing with the case of violent re-virialisation: the GCs become much more radially anisotropic if they collapse violently. This is very clear from comparing the lower panels

of Figures 7 and 14. For model 2,  $\beta(r_{90}) = 0.8$  for violent compression and  $\beta(r_{90})$  is only 0.4 for adiabatic compression. For the most diffuse models 3 and 5 this is even more significant: values of  $\beta(r_{90})$  are 0.85 – 0.90 for violent re-virialisation while the values of  $\beta(r_{90})$  are only 0.45 – 0.6 for adiabatic compression. The more compact models (model 1 and 4) have the same trend although not as significant as model 2, since among the three models, model 2 itself is in deeper MD.

Moreover, the final  $\beta(r)$  profiles for different GCs are independent of the Galactic orbits. There is only one exception, model 3, for which the difference in anisotropy,  $\delta\beta(r_{90})$  is up to 0.2. The large  $\delta\beta(r_{90})$  comes from there being fewer particles for model 3 therefore the particle noise is larger.

Thus the anisotropy profiles are related to the internal structures of the GCs. The faster the systems move from the inner to the outer Galaxy, the more radially anisotropic the systems are. However, both the  $\sigma_r(r)$  profiles and the  $\beta(r)$  profiles are not related to the orbital history. I.e., the internal kinematics of a GC, which is moving on an eccentric Galactic orbit and is currently in the Milgromian regime, only depends on the internal structure of the GC rather than on the details of the orbital history. This is good news, and it makes the predictions from Milgromian dynamics less complex.

#### 4.4.4 Phase space distribution with adiabatic re-virialisation

The phase space distributions of systems with adiabatic re-virialisation are presented in Fig. 15, which can be compared with the case of violent re-virialisation. One Galactic orbit is selected from Fig. 11, the purple curve, i.e. the initial Galactic position for the cluster is at  $r_{\text{MW}} = 5 \text{ kpc}$  and the initial velocity is  $500 \text{ km s}^{-1}$ . We show in Fig. 15 the models 4 (left panels), 2 (middle panels) and 5 (right panels) at time snapshots of  $0.5 T_{\text{cross}}^{\text{MD}}$ ,  $1.0 T_{\text{cross}}^{\text{MD}}$ ,  $17 T_{\text{cross}}^{\text{MD}}$  and the apocentre of the Galactic orbit (or the furthest position that Milky Way star clusters are observed, say, 90 kpc away to

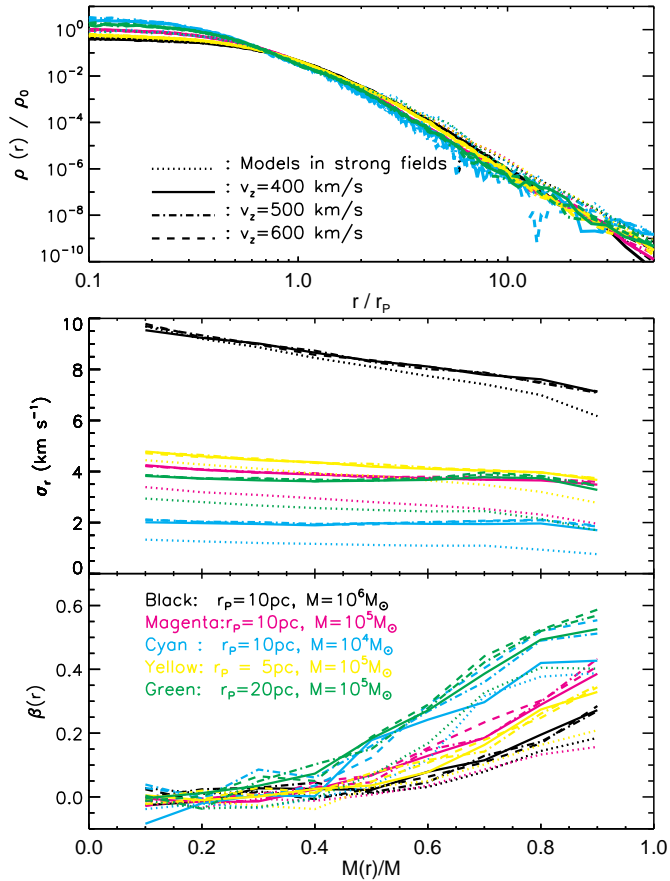


**Figure 14.** The spherically averaged density  $\rho(r)$  (upper panel)  $\sigma_r(r)$  (middle panel) and anisotropic profiles  $\beta(r)$  (lower panel) for models 1 (black), 2 (magenta) and 4 (yellow) in a strong external field (dotted curves) and in weak fields. The systems move on radial polar orbits of the Galaxy, with different initial velocities, the line types showing the state of the systems at their apocentres:  $v_z = 400 \text{ km s}^{-1}$  (solid),  $500 \text{ km s}^{-1}$  (dot-dashed) and  $600 \text{ km s}^{-1}$  (dashed). The colours and line types are defined as in Fig. 12.

the Galactic centre). At the early stage of re-virialisation, the systems appear to be well phase mixed. Only for the deep-Milgromian system, model 5, there are structures with negative radial velocity in the outer regimes of  $r > 5 r_P$ , which indicates that a large amount of particles are falling into the centre of the star cluster. The reason is that, on a realistic Galactic orbit, the self-potential of the star cluster does not change to a sufficiently significant extent during one crossing time of the cluster. Only when the star cluster has a very diffuse mass distribution and the self-potential is dominated by deep-Milgromian dynamics, a small amount of change of the background external field is able to yield a visible effect in the phase space distribution. The systems are already well phase mixed at  $17 T_{\text{cross}}^{\text{MD}}$ , and the phase space distributions are very close to that of the final time snapshot, namely at the furthest Galactic position where the star cluster can reach (the bottom panels of Fig. 15).

There is a wide range for the initial conditions of Galac-

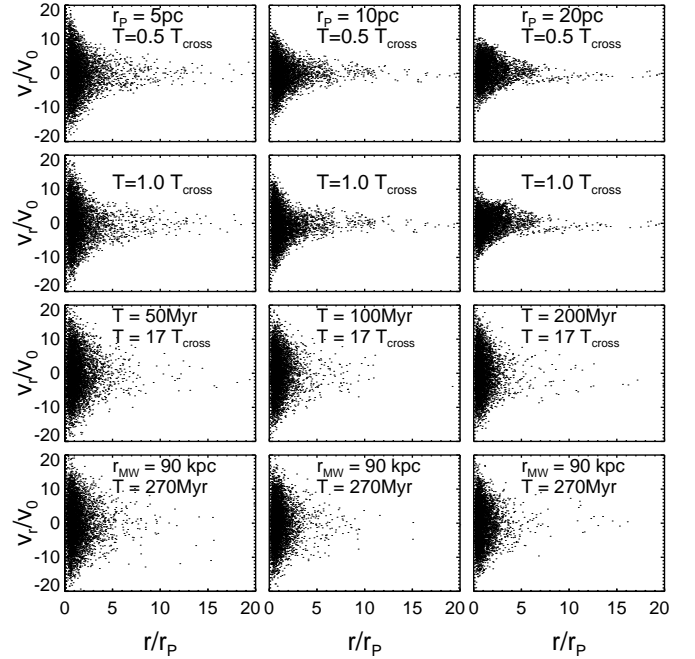


**Figure 15.** The phase space distribution at different snapshots of adiabatic re-virialisation for models 4 (left panels), 2 (middle panels) and 5 (right panels) moving on a Galactic orbit with initial position of 5 kpc and initial velocity of  $500 \text{ km s}^{-1}$  (purple curves in Fig. 11, for model 5 the Galactic orbit is the same one but the starting point is 10 kpc and the initial velocity is interpolated from the purple curve in the right panel of Fig. 11). The radial radii are scaled by the Plummer radius  $r_P$ , and the radial velocity of particles  $v_r$  are scaled by  $v_0 = \sqrt{GM/r_P}$ .

tic orbits for the GCs. Thus it is important to study the phase space distribution for GCs on different Galactic orbits. Model 2 is presented on different Galactic orbits with different initial velocities in Fig. 16:  $400 \text{ km s}^{-1}$  (left panels),  $500 \text{ km s}^{-1}$  (middle panels) and  $600 \text{ km s}^{-1}$  (right panels). On an orbit with higher initial velocity, it is clear there are in-falling particles at an early stage of  $T = 1.0 T_{\text{cross}}^{\text{MD}}$ . The systems are already well phase mixed at  $17 T_{\text{cross}}^{\text{MD}}$ , although the GCs are still moving on the orbits. It agrees with the results of GCs with different sizes moving on a same orbit in Fig. 15.

We therefore conclude that, for the systems re-virialised adiabatically, the phase mixing is more efficient than that in the violent re-virialisation process. The self-potentials for GCs are mildly deepened in the former case, because the systems are very close to being in equilibrium on the orbits.

#### 4.4.5 Stability of the star clusters after adiabatic re-virialisation

The study of the anisotropy of the systems reveals that GCs are less radially anisotropic through adiabatic re-virialisation compared to that realized through violent re-virialisation. It is therefore reasonable to expect  $\xi$  parameters (Eq. 8) to be smaller for the systems adiabatically re-virialised. The values of  $\xi$  for GCs re-virialised on different Galactic orbits are listed in Table 3. For all the models  $\xi < \xi_c$

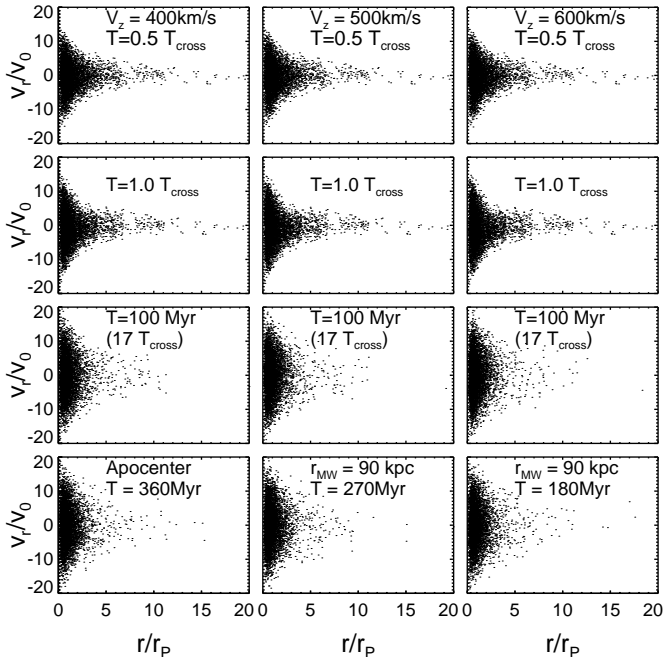


**Figure 16.** The phase space distribution at different snapshots of adiabatic re-virialisation for model 2 moving on different Galactic orbit with initial position of 5 kpc and initial velocity of  $400 \text{ km s}^{-1}$  (left panels),  $500 \text{ km s}^{-1}$  (middle panels) and  $600 \text{ km s}^{-1}$ . The radial radii are scaled by the Plummer radius  $r_P$ , and the radial velocity of particles  $v_r$  are scaled by  $v_0 = \sqrt{GM/r_P}$ .

(The critical  $\xi_c$  values in Milgromian dynamics is empirically calculated in Nipoti et al. 2011). Apparently, all the GC systems are stable after adiabatic re-virialisation. It can also be found from Table 3 that for the more compact GCs (Models 1, 2 and 4), the  $\xi$  values are very similar to each other on different Galactic orbits. For the more diffuse GCs (Models 3 and 5) which re-virialised into deep-Milgromian gravity, the difference of  $\xi$  values are more significant on different Galactic orbits. For systems with larger initial velocity, the  $\xi$  values are larger, which is owing to the presence of more radial orbits in the systems which re-virialised more rapidly. These results agree well with the analysis of anisotropy in §4.4.3.

The values of  $\xi$  for GCs after adiabatic re-virialisation are smaller than those in the case of violent re-virialisation, suggesting that adiabatically re-virialised GCs are even more stable.

## 5 CONCLUSIONS AND DISCUSSIONS

We study the violent and adiabatic re-virialisation of stellar systems from Newtonian to Milgromian gravity. The time scale of the re-virialisation is only a few crossing times in MD, for both the violent and the adiabatic process. Therefore it would be unlikely to find systems like diffuse GCs or ultra faint dwarf galaxies that are in a weak background field regime to be frozen in Newtonian dynamics. There are GCs like Pal 4 (Frank et al. 2012), Pal 14 (Jordi et al.

2009) and NGC 2419 (Baumgardt et al. 2009; Ibata et al. 2011a,b), which at first sight appear to be Newtonian diffuse systems in the outer Galactic regime. We conclude that this behaviour cannot be explained by these systems being frozen in Newtonian gravity. The adiabatic simulations show that the orbital time is much longer than the dynamical times  $T_{\text{dyn}}^i$  of the systems staying out of equilibrium. A more recent study on NGC 2419 (Sanders 2012a,b) shows that NGC 2419 is not a problem for MD. Sanders (2012a,b) used polytropic models to model NGC 2419, which fit well the observations of the surface brightness and kinematics. However Ibata et al. (2011b) claimed that polytrope models are less likely in Milgromian dynamics by a factor of 5000 than a Newtonian Michie model as used in Ibata et al. (2011a). Therefore currently NGC2419, Pal 4 and Pal 14 cannot be explained by the potential being frozen in its Newtonian form.

We also study the Lagrangian radii, mass profiles and kinematics of the final products for the above two re-virialisation process. We find that the mass profiles and radial velocity dispersion profiles are very similar for the systems collapsing the two different ways. Moreover, different Galactic orbits for a GC lead to the same Lagrangian radii,  $\rho(r)$  and  $\sigma_r(r)$  profiles. Therefore for a system moving from the inner regime of the Galaxy to the outer part, the Lagrangian radii, mass profile and  $\sigma_r(r)$  are independent of the history of the GC's orbit.

In the potential of the Galaxy, we revirialise the spherically symmetric Newtonian systems in the inner Galactic field using Milgromian dynamics. The velocity dispersion becomes radially anisotropic after the re-virialisation due to the external field effect: since the SEP is broken, the internal potential of a GC is asymmetric, therefore the orbits of the particles in such a GC are distorted and elongated. We then move the GCs from the inner to the outer regime of the Galaxy. We find that in those GCs, the velocity dispersion profiles should evolve to even more radially anisotropic profiles. Note that the  $\beta(r)$  profiles are determined by the internal structure of the GCs rather than by the details of the Galactic orbits: the more diffuse the GCs are, the more radially anisotropic their velocity dispersions are after the re-virialisation. The GCs on an orbit moving faster or slower from the Newtonian regime to the Milgromian regime have similar radially anisotropic velocity dispersion profiles. The re-virialisation is a new mechanism to produce such profiles compared to Newtonian dynamics. In contrast, Newtonian N-body models of star clusters generate isotropic or mildly anisotropic velocity dispersion profiles.

Observations of the distant GCs NGC 2419 by Baumgardt et al. (2009) and Ibata et al. (2011a,b) show that the line-of-sight velocity dispersion profile of NGC 2419 has large values up to  $7 \text{ km s}^{-1}$  in the centre and small values of  $1 - 2 \text{ km s}^{-1}$  in the outer regime where  $r > 3r_h$  (see Fig. 8 of Ibata et al. 2011a). The studies on the dynamics of NGC 2419 require a highly radially anisotropic velocity dispersion to fit the observed data in both Newtonian or Milgromian gravities (Ibata et al. 2011a,b). In Newtonian dynamics, one mechanism to generate such radial anisotropy is partial relaxation, i.e. a violent relaxation process that is inefficient in the outer parts of the system (Lynden-Bell 1967; Bertin & Trenti 2003). A self-consistent family of radially anisotropic models of partially relaxed systems have

**Table 3.** The stability parameter  $\xi$  for the GC models adiabatically re-virialised from the Galactocentric positions  $((0, 0, 5)$  kpc for models 1, 2 and 4, and  $(0, 0, 10)$  kpc for models 3 and 5) to the outer regime of the Milky Way. The second to the fourth columns show the values of  $\xi$  of the clusters moving on different Galactic orbits.

Models	Apocentre $v_z = 400 \text{ km s}^{-1}$	$r^{\text{MW}} = 90 \text{ kpc}$ $v_z = 500 \text{ km s}^{-1}$	$r^{\text{MW}} = 90 \text{ kpc}$ $v_z = 600 \text{ km s}^{-1}$
1	1.09	1.09	1.09
2	1.16	1.17	1.19
3	1.24	1.32	1.35
4	1.12	1.12	1.13
5	1.29	1.34	1.36

been proposed in Bertin & Trenti (2003). Later, Trenti et al. (2005) compared such a family of models and the products of collisionless collapse. It was confirmed that these models are unstable while the stability parameter  $\xi > 1.7 \pm 0.25$  in Newtonian dynamics, and that the strongly radial models will evolve into triaxial systems. Recently, Zocchi et al. (2012) investigated these models for a sample of GCs including NGC 2419. The stability parameter is found to be  $\xi = 1.77$  for the best fit model of NGC 2419, so NGC 2419 is on the boundary of being stable in Newtonian dynamics.

The phase transition provides another mechanism for generating the anisotropy in Milgromian dynamics, in addition to the partial relaxation which has not yet been studied in Milgromian dynamics.

Here we also show the final line-of-sight velocity dispersion profiles,  $\sigma_{LOS}(R)$ , of our GC models after moving from the inner Galaxy to the outer Galactic regime (Fig. 17). Since our GC models are radially anisotropic, especially for models 2, 3 and 5, the shapes of their  $\sigma_{LOS}(R)$  should be similar to that of NGC 2419. Indeed we find that the  $\sigma_{LOS}(R)$  have large values in the centres of the GCs and sharply fall from  $1r_P$  to  $10r_P$ . The  $\sigma_{LOS}(R)$  profiles are very similar for the same model moving on different Galactic orbits (see Fig. 17). It confirms that the observational results of line-of-sight kinematics of a GC are not related to the orbital history.

In a follow-up project we will study other possible mechanisms for generating radially anisotropic velocity dispersion profiles and the corresponding  $\sigma_{LOS}(R)$  profiles in both MD and Newtonian gravities. For instance, it is interesting to consider gas expulsion after birth and mass loss from evolving mass stars in the early stage of the GCs (Marks & Kroupa 2012, for initial conditions of GCs) and make a comparison between the different radial anisotropic behaviours generated from Newtonian and Milgromian gravities.

In summary, Milgromian dynamics predicts that all of the GCs moving on eccentric orbits of the Galaxy should be radially anisotropic when they are in the Milgromian regime. Any isotropic or tangentially anisotropic profiles for GCs in the outer regime of any radial Galactic orbit will be problematic for MD, since these systems experience a collapse during the phase transition. Therefore for any out-going systems, any observations on isotropy or tangential anisotropy will be a severe challenge to MD. MD is falsifiable by the kinematics of the outer GCs.

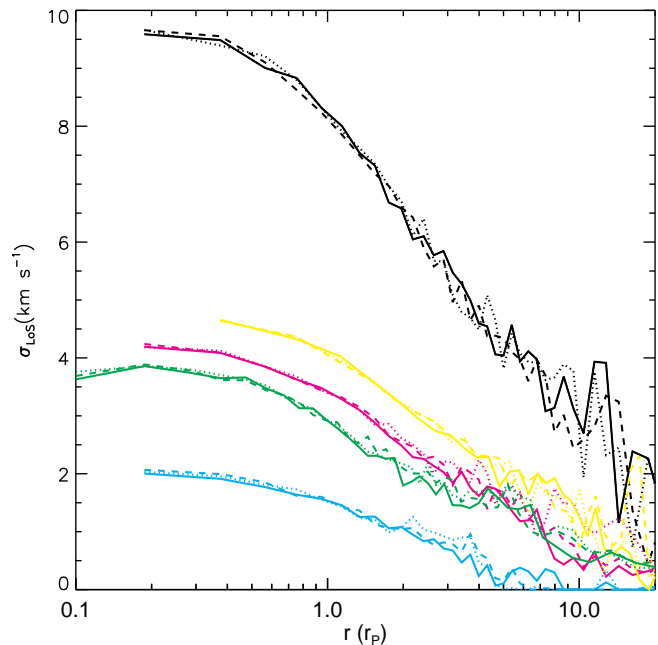


**Figure 17.** The final line-of-sight velocity dispersion profiles as a function of radius for the models after moving from the inner Galaxy to the outer Milgromian regime. The colours and line types are defined as in Fig. 12.

## 6 ACKNOWLEDGMENTS

Xufen Wu gratefully acknowledges support through the Alexander von Humboldt Foundation. We thank Ortwin Gerhard and Flavio de Lorenzi for sharing the code for generating anisotropic models by using circularity functions and Lucy's method. We also thank the Bologna group, Nipoti, Ciotti and Londrillo for sharing their N-body code NMODY.

## APPENDIX A: STABILITY TEST OF UNPERTURBED NEWTONIAN INITIAL CONDITIONS (ICS)

We freely evolve the Newtonian ICs constructed in §2 in their self-potentials. Fig. A1 shows the scalar virial ratios  $2K/|W|$  of the models evolving for about  $25 T_{\text{cross}}^{\text{Newt}}$ . We find that the virial ratios are always around 1 with small per-

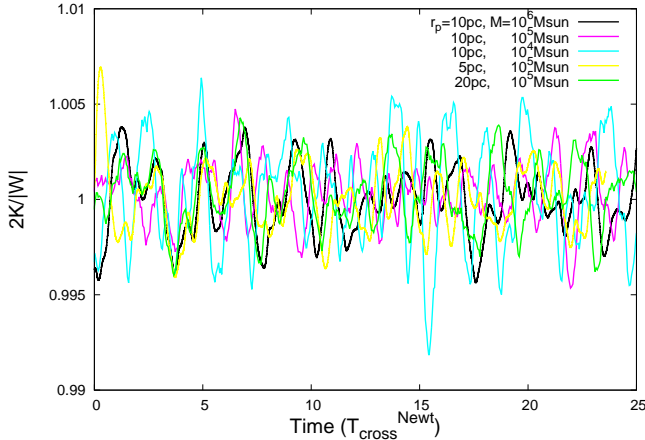


**Figure A1.** The virial ratio during the free evolution of the Newtonian models.

turbations of amplitude  $\delta(2K/|W|) < 1\%$ . The models are therefore in virial equilibrium.

We further show the spherically averaged density profiles of the models before (dotted lines) and after (dashed lines) the phase mixing in the upper panel of Fig. A2, as well as their radial velocity dispersion (middle panel) and anisotropy profiles (lower panel, Eq. 7). We find that their density, radial velocity dispersion and anisotropy profiles do not evolve with time. The models are still isotropic models after  $25 T_{\text{cross}}^{\text{Newt}}$  and their spatial and velocity distributions do not change. Thus we conclude that the phase space distribution functions of the models do not evolve during the free evolution, and the models are stable. This is expected for collisionless systems.

## REFERENCES

- Angus G. W., 2009, MNRAS, 394, 527  
 Angus G. W., Diaferio A., 2011, MNRAS, 417, 941  
 Angus G. W., Famaey B., Tiret O., Combes F., Zhao H. S., 2008, MNRAS, 383, L1  
 Baumgardt H., Côté P., Hilker M., Rejkuba M., Mieske S., Djorgovski S. G., Stetson P., 2009, MNRAS, 396, 2051  
 Baumgardt H., Grebel E. K., Kroupa P., 2005, MNRAS, 359, L1  
 Baumgardt H., Makino J., 2003, MNRAS, 340, 227  
 Bekenstein J., Milgrom M., 1984, ApJ, 286, 7  
 Bellazzini M., 2007, A&A, 473, 171  
 Bertin G., Trenti M., 2003, ApJ, 584, 729  
 Bienaymé O., Famaey B., Wu X., Zhao H. S., Aubert D., 2009, A&A, 500, 801  
 Binney J., Tremaine S., 2008, Galactic Dynamics: Second Edition. Princeton University Press  
 Bruens R. C., Kroupa P., 2012, ArXiv e-prints, 1209.4353  
 Brüns R. C., Kroupa P., 2011, ApJ, 729, 69  
 Chandar R., Whitmore B., Lee M. G., 2004, ApJ, 611, 220  
 Chies-Santos A. L., Santiago B. X., Pastoriza M. G., 2007, A&A, 467, 1003

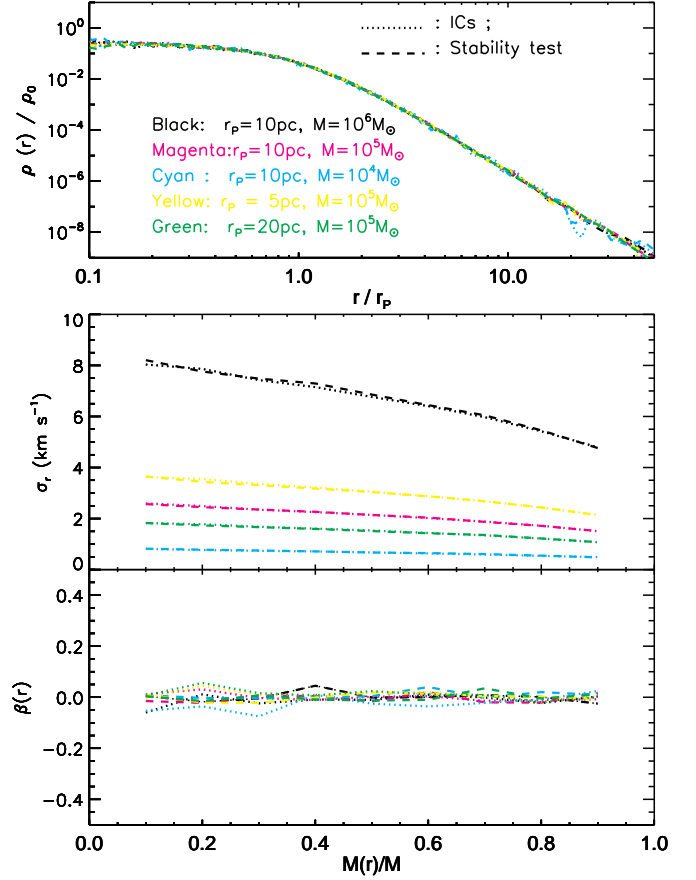


**Figure A2.** The spherically averaged density (upper panel), radial velocity dispersion (middle panel) and anisotropy profiles (lower panel) for models in Table 1. The dotted and dashed lines are for ICs and the models which are evolved for about  $25 T_{\text{cross}}^{\text{Newt}}$  in Newtonian gravity.

- Clausius R., 1870, De la fonction potentielle DU Potentiel. Paris : Gauthier-Villars, 1870; XIV, 141 p. ; in 8.; DCCC.4.398  
 Famaey B., Binney J., 2005, MNRAS, 363, 603  
 Famaey B., Bruneton J.-P., Zhao H., 2007, MNRAS, 377, L79  
 Famaey B., McGaugh S., 2011, ArXiv e-prints, 1112.3960  
 Frank M. J., Hilker M., Baumgardt H., Côté P., Grebel E. K., Haghi H., Küpper A. H. W., Djorgovski S. G., 2012, ArXiv e-prints, 1205.2693  
 Gentile G., Famaey B., Angus G., Kroupa P., 2010, A&A, 509, A97  
 Gentile G., Famaey B., Combes F., Kroupa P., Zhao H. S., Tiret O., 2007, A&A, 472, L25  
 Gentile G., Famaey B., Zhao H., Salucci P., 2009, Nature, 461, 627  
 Georgiev I. Y., Puzia T. H., Hilker M., Goudfrooij P., 2009, MNRAS, 392, 879  
 Gerhard O. E., 1983, MNRAS, 202, 1159  
 Gerhard O. E., 1991, MNRAS, 250, 812  
 Giersz M., Heggie D. C., 1997, MNRAS, 286, 709  
 Haghi H., Baumgardt H., Kroupa P., 2011, A&A, 527, A33

- Haghi H., Baumgardt H., Kroupa P., Grebel E. K., Hilker M., Jordi K., 2009, MNRAS, 395, 1549
- Harris W. E., 1996, AJ, 112, 1487
- Harris W. E., Harris G. L. H., Holland S. T., McLaughlin D. E., 2002, AJ, 124, 1435
- Hilker M., 2006, A&A, 448, 171
- Huxor A. P., Ferguson A. M. N., Tanvir N. R., Irwin M. J., Mackey A. D., Ibata R. A., Bridges T., Chapman S. C., Lewis G. F., 2011, MNRAS, 414, 770
- Ibata R., Sollima A., Nipoti C., Bellazzini M., Chapman S. C., Dalessandro E., 2011a, ApJ, 743, 43
- Ibata R., Sollima A., Nipoti C., Bellazzini M., Chapman S. C., Dalessandro E., 2011b, ApJ, 738, 186
- Iorio L., 2010, The Open Astronomy Journal, 3, 156
- Jordi K., Grebel E. K., Hilker M., Baumgardt H., Frank M., Kroupa P., Haghi H., Côté P., Djorgovski S. G., 2009, AJ, 137, 4586
- Kroupa P., 2012, Publications of the Astronomical Society of Australia, 29, 395
- Kroupa P., Famaey B., de Boer K. S., Dabringhausen J., Pawlowski M. S., Boily C. M., Jerjen H., Forbes D., Hensler G., Metz M., 2010, A&A, 523, A32
- Kroupa P., Pawlowski M., Milgrom M., 2012, International Journal of Modern Physics D, 21, 30003
- Larsen S. S., Brodie J. P., 2000, AJ, 120, 2938
- Lee K. H., Lee H. M., Sung H., 2006, MNRAS, 367, 646
- Lee M. G., Chandar R., Whitmore B. C., 2005, AJ, 130, 2128
- Londrillo P., Nipoti C., 2009, Memorie della Societa Astronomica Italiana Supplement, 13, 89
- Lüghausen F., Famaey B., Kroupa P., Angus G., Combes F., Gentile G., Tiret O., Zhao H., 2013, MNRAS
- Lynden-Bell D., 1967, MNRAS, 136, 101
- Marks M., Kroupa P., 2012, A&A, 543, A8
- Milgrom M., 1983, ApJ, 270, 365
- Milgrom M., 1999, Physics Letters A, 253, 273
- Milgrom M., 2009, MNRAS, 399, 474
- Milgrom M., Sanders R. H., 2003, ApJ, 599, L25
- Nipoti C., Ciotti L., Binney J., Londrillo P., 2008, MNRAS, 386, 2194
- Nipoti C., Ciotti L., Londrillo P., 2011, MNRAS, 414, 3298
- Nipoti C., Londrillo P., Ciotti L., 2007, ApJ, 660, 256
- Peng E. W., Côté P., Jordán A., Blakeslee J. P., Ferrarese L., Mei S., West M. J., Merritt D., Milosavljević M., Tonry J. L., 2006, ApJ, 639, 838
- Plummer H. C., 1911, MNRAS, 71, 460
- Polyachenko V. L., Shukhman I. G., 1981, Soviet Ast., 25, 533
- Radburn-Smith D. J., Lucey J. R., Woudt P. A., Kraan-Korteweg R. C., Watson F. G., 2006, MNRAS, 369, 1131
- Robin A. C., Reylé C., Derrière S., Picaud S., 2003, A&A, 409, 523
- Sanders R. H., 2012a, MNRAS, 419, L6
- Sanders R. H., 2012b, MNRAS, 422, L21
- Sanders R. H., Noordermeer E., 2007, MNRAS, 379, 702
- Takahashi K., Lee H. M., 2000, MNRAS, 316, 671
- Trenti M., Bertin G., 2006, ApJ, 637, 717
- Trenti M., Bertin G., van Albada T. S., 2005, A&A, 433, 57
- Tully R. B., Fisher J. R., 1977, A&A, 54, 661
- Wu X., Famaey B., Gentile G., Perets H., Zhao H., 2008, MNRAS, 386, 2199
- Wu X., Zhao H., Famaey B., 2010, JCAP, 6, 10
- Wu X., Zhao H., Famaey B., Gentile G., Tiret O., Combes F., Angus G. W., Robin A. C., 2007, ApJ, 665, L101
- Zhao H. S., Tian L., 2006, A&A, 450, 1005
- Zocchi A., Bertin G., Varri A. L., 2012, A&A, 539, A65